CHALMERS
UNIVERSITY OF TECHNOLOGY

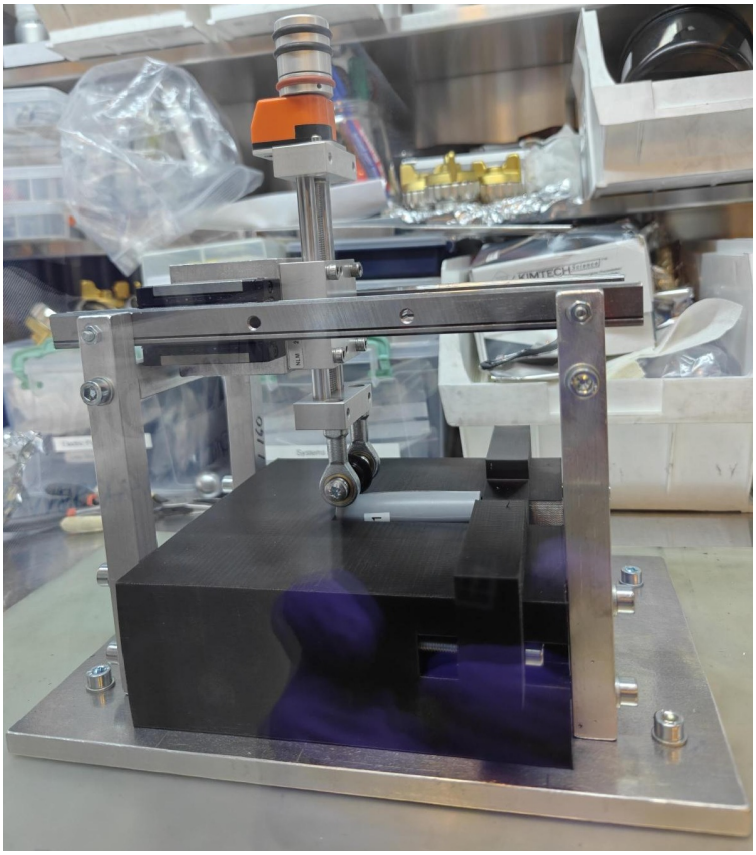

Ageing behaviour of a commercial 18650 Li-ion cell with a SiO_x-containing negative electrode

Master's thesis in Materials Chemistry

LIAM EKMAN

DEPARTMENT OF ELECTRICAL ENGINEERING

CHALMERS UNIVERSITY OF TECHNOLOGY
Gothenburg, Sweden 2026
www.chalmers.se

Master's thesis EENX30 2026

Ageing behaviour of a commercial 18650 Li-ion cell with SiO_x-containing negative electrode

LIAM EKMAN

CHALMERS
UNIVERSITY OF TECHNOLOGY

Department of Electrical Engineering
Division of Electric Power Engineering
Chalmers University of Technology
Gothenburg, Sweden 2026

Ageing behaviour of a commercial 18650 Li-ion cell with SiO_x-containing negative electrode
LIAM EKMAN

Supervisor: Dr. Anna Tomsic, Micropower
Dr. Nareerat Plylahan, Micropower
Dr. Ritambhara Gond, Department of Electrical Engineering
Examiner: Dr. Evelina Wikner, Department of Electrical Engineering

Master's Thesis 2026
Department of Electrical Engineering
Division of Electric Power Engineering
Chalmers University of Technology
SE-412 96 Gothenburg
Telephone +46 31 772 1000

Cover: Teardown of cell 11 conducted inside a glovebox using an in-house developed tool.

Typeset in LaTeX
Printed by Chalmers Reproservice
Gothenburg, Sweden 2026

Ageing behaviour of a commercial 18650 Li-ion cell with SiO_x-containing negative electrode

LIAM EKMAN
Department of Electrical Engineering
Chalmers University of Technology

Abstract

This thesis investigated the cycling performance and ageing behaviour of commercial 18650 Li-ion cells with a SiO_x-containing negative electrode. Lifetime testing was conducted under different voltage window placements, voltage window widths, and charge C-rates to evaluate the influence of operating conditions on cell ageing. Electrochemical characterisation included capacity measurements, incremental capacity analysis (ICA), and electrochemical impedance spectroscopy (EIS). Non-destructive characterisation was performed using computed tomography (CT), while post-mortem analysis included scanning electron microscopy (SEM), energy dispersive X-ray spectroscopy (EDX), and laboratory-scale PAT-cells.

The results demonstrated that voltage window placement had a greater influence on ageing than voltage window width or charge C-rate under the investigated conditions. Cells cycled within a centred voltage window exhibited comparatively mild degradation, whereas cells cycled closer to the upper or lower voltage limits showed significantly more severe ageing behaviour. In particular, cells cycled at lower voltage limit exhibited substantially faster capacity fade despite operating within similar voltage window widths. The degradation was primarily associated with the negative electrode and was linked to high delithiation, Li-plating, SEI instability, mechanical degradation, and loss of cyclable lithium.

Post-mortem analysis revealed heterogeneous ageing across the jellyroll, where the inner, middle, and outer electrode regions exhibited different degradation behaviour. Electrochemical characterisation through ICA and EIS revealed increased resistance, peak broadening, peak shifts, and increased polarisation with ageing, consistent with interfacial degradation and non-uniform lithiation. Furthermore, visible Li-plating was not directly proportional to capacity fade, indicating that irreversible degradation processes contributed significantly to the ageing behaviour.

In addition, an in-house developed teardown tool significantly reduced the cell disassembly time. However, the cutting process damaged the outer three jellyroll layers, indicating that further refinement of the tool design is required.

Keywords: Li-ion battery, silicon oxide, ageing, voltage window placement, teardown, electrochemistry, post-mortem analysis.

Acknowledgement

I would like to express my sincere gratitude to my supervisors, Dr. Anna Tomsic, Dr. Nareerat Plylahan, and Dr. Ritambhara Gond, together with my examiner, Dr. Evelina Wikner, for their encouragement, guidance, and support throughout this master's thesis. I am especially grateful to Dr. Wikner for her unwavering support throughout this work; her availability and willingness to engage in problem solving made even the most challenging phases manageable. I also deeply appreciate the trust and insightful feedback provided by Dr. Tomsic and Dr. Plylahan at Micropower, as well as Dr. Gond's invaluable support during the laboratory work and her expertise in SEM measurements.

This thesis would not have been possible without the financial support of Micropower and Chalmers University of Technology, whose contributions are gratefully acknowledged.

I am also indebted to Dr. Douglas Jutsell Nilsson for his dedication to the design and production of the tool, and to Mr. Leopold Werberg from Volvo Cars for his assistance with the CT scans. I am grateful to Dr. Amanda Persdotter and Dr. Antonio Mulone for their guidance and support with the SEM instrument, and to Dr. Kristian Bartholdsson Fernander for generously sharing his expertise in Python programming and providing valuable technical insights.

Gothenburg, June 2026
Liam Ekman

List of Acronyms

The following is the list of acronyms that have been used throughout this thesis listed in alphabetical order:

BOL	Beginning Of Life
BSE	Backscattered Electrons
CAD	Computer-Aided Design
CCCV	Constant Current - Constant Voltage
CT scan	Computed Tomography scan
DOD	Depth Of Discharge
EDX	Energy Dispersive X-ray spectroscopy
EOL	End Of Life
ESW	Electrochemical Stability Window
FCE	Full Cycle Equivalent
FDM	Fused Deposition Modelling
HPPC	Hybrid Pulse Power Characterisation
ICA	Incremental Capacity Analysis
ICI	Intermittent Current Interruption
LiB	Lithium-ion Battery
NMC	Lithium Nickel Manganese Cobalt Oxide (positive electrode)
OCV	Open-Circuit Voltage
PAT-cell	Parallel Testing (efficient test cell system developed by the company EL-CELL)
PP	Polypropylene
RPT	Reference Performance Test
SE	Secondary Electrons
SEI	Solid Electrolyte Interphase
SEM	Scanning Electron Microscopy
SHE	Standard Hydrogen Electrode
SOC	State Of Charge
SOH	State of Health
TC	Test condition

Nomenclature

The following is the nomenclature of the parameters and variables that have been used throughout this thesis.

Parameters

F	Faraday constant ($96\,485.3321\,\mathrm{Cmol}^{-1}$)
E^0	Absolute standard electrode potential
R	The universal gas constant ($8.3143\,\mathrm{Jmol}^{-1}\mathrm{K}^{-1}$)
E_0	Initial potential
I_0	Initial current
In_0	Initial beam intensity
k	Diffusion resistance coefficient
σ	The diffusion coefficient
μ	Linear attenuation coefficient

Variables

ΔG	Gibbs free energy
E_{cell}	Cell potential
n	Number of electrons transferred
a_+, a_-	Activities of the oxidised and reduced species
E_{Fneg}	The negative electrode's Fermi level
E_{Fpos}	The positive electrode's Fermi level
η_{ct}	Activation polarisation
η_c	Concentration polarisation
I	Current
R_{cell}	Internal resistance

Q	Capacity
Q_{TP}	Discharge capacity throughput
Q_N	Nominal battery capacity
$C - rate$	The current divided by the nominal capacity
Q_n	Available capacity
ω	Angular frequency
ϕ	Phase shift
$Z(\omega)$	Impedance
R_s	Bulk electrolyte resistance
R_{ct}	Charge transfer resistance
ω_{max}	The angular frequency at the peak of the semicircle in a Nyquist plot
C_{dl}	Double-layer capacitance
In	Detected beam intensity
x	Thickness of the material (the length of the photon's path through the sample)

Table of Contents

1
Introduction

1.1 Background

To address the continued rise in greenhouse gas emissions, particularly carbon dioxide (CO_2), it is imperative to reduce and ultimately phase out the use of fossil fuels. The transportation sector is the second largest contributor to global carbon emissions after the power sector, making its decarbonisation essential for achieving climate neutrality goals. In this context, renewable energy carriers such as hydrogen and electricity play a key role in enabling the transition to hydrogen powered and electric vehicles [1][2].

Lithium-ion batteries (LiBs) are widely used for energy storage across transportation, consumer electronics, and large scale systems [3]. The design of electric vehicle batteries spans multiple disciplines, including materials science, electrochemistry, thermodynamics, dynamic modelling, control systems, and electrical and mechanical engineering [4]. This study focuses on the materials science and electrochemical aspects of commercial LiBs.

This master's thesis was conducted in collaboration with Micropower and Chalmers University of Technology. Micropower develops industrial LiBs, chargers, and power converters for industrial vehicles. With over 40 years of experience, the company has a strong industrial track record. In recent years, Micropower has delivered more than 300 MWh of battery systems annually and increased charging system production capacity to 270,000 units per year, scaled across multiple markets. The company currently operates in-house R&D and manufacturing facilities in the Nordics, as well as battery pack assembly sites in Germany and the United States [5].

Li-ion cells with silicon oxide (SiO_x)-containing negative electrodes offer high energy density and fast charging capability. However, the significant volume changes of SiO_x during cycling lead to rapid capacity fading and reduced cycle life. Improvements can be achieved by optimising SiO_x morphology, adjusting its content in graphite electrodes, or defining an appropriate voltage window. Therefore, this thesis investigates the influence of charge C-rate, voltage window width, and voltage window placement on cell ageing. Cells undergo lifetime cycling combined with reference performance tests (RPTs), followed by disassembly of fresh and aged cells to analyse changes in electrochemical performance. Experimental work, including cycling, teardown, and PAT-cell preparation, was conducted at Chalmers University of Technology. CT scans were performed at Volvo Cars, while SEM and EDX analyses were carried out at the Department of Materials Science, Chalmers.

1.2 Aim

The aim of this thesis is to investigate the influence of charge C-rate, voltage window placement, and voltage window width on the ageing behaviour of commercial 18650 Li-ion cells with a SiO_x-containing negative electrode and an NMC positive electrode. The study focuses on identifying the dominant degradation mechanisms associated with different operating conditions and evaluating how these mechanisms affect the electrochemical performance of the cells. To achieve this aim, lifetime testing was conducted at room temperature (28 °C) under different cycling conditions. Periodic reference performance tests (RPTs) were performed throughout ageing and included capacity measurements, hybrid pulse power characterisation (HPPC), and intermittent current interruption (ICI) measurements for incremental capacity analysis (ICA). In addition, an in-house developed tool for opening cylindrical cells with stainless steel casings was designed to enable efficient post-mortem analysis. Non-destructive characterisation was performed using computed tomography (CT), while post-mortem characterisation included cell teardown, scanning electron microscopy (SEM), energy-dispersive X-ray spectroscopy (EDX), and electrochemical characterisation of laboratory-scale PAT-cells.

1.3 AI

Artificial intelligence (AI) tools, including ChatGPT, were used throughout the thesis to assist with language refinement and grammatical corrections. AI was also used to support segments of the coding process, including debugging and data analysis script development. All scientific interpretations, analyses, and conclusions were evaluated and verified by the author.

2
Theory

2.1 The lithium ion battery cell

An electrochemical cell is the fundamental unit of a battery, enabling the conversion of chemical energy to electrical energy during discharge, and vice versa during charging. Electrochemical cells are classified as either electrolytic or galvanic. In electrolytic cells, electrical energy drives a non-spontaneous chemical reaction ($\Delta G > 0$), storing energy, the charging process. In galvanic cells, a spontaneous reaction ($\Delta G < 0$) releases stored chemical energy as electrical energy during discharge [4].

An electrochemical cell consists of electrodes and electrolyte. To make an electrochemical cell into a functioning battery additional components are needed, such as current collectors, separator and an outer casing. During charge and discharge, redox reactions occur at both electrodes, with electrons flowing through an external circuit and ions moving through the electrolyte to maintain charge balance. During discharge the negative electrode undergoes oxidation (electron release), while the positive electrode undergoes reduction (electron acceptance), as illustrated in Figure 2.1. The electrodes are porous to enhance the efficiency and reversibility of these reactions. Current collectors, typically aluminium foils for the positive electrode and copper foils for the negative electrode, enable electron transport and contribute to the dissipation of heat generated during operation. The electrolyte serves as the medium for ionic conduction between electrodes, while the separator prevents direct contact between them, thereby reducing the risk of internal short circuits. The separator must be electronically insulating yet allow efficient ionic movement. It typically consists of a porous membrane pre-soaked with electrolyte. The cell casing ensures mechanical stability, prevents electrolyte evaporation, and enhances the long-term safety of the cell. Casings are manufactured from various materials, such as plastics or metals, and can be either rigid or flexible depending on the application [4][6].

During research and development, it is advantageous to study electrodes individually by dividing a full electrochemical cell into two half-cells. Metallic lithium is often used as a counter electrode due to its well-defined potential. This configuration

allows the electrode of interest to be investigated against lithium, aiding the study of degradation mechanisms through post-mortem analysis of aged cells. However, to examine interactions between all cell components, full cell studies, consisting of both positive and negative electrodes, remain essential [4].

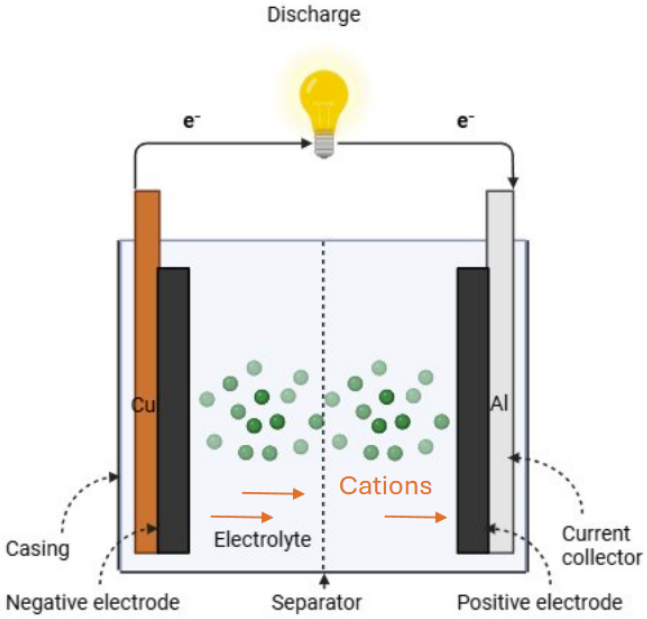

Figure 2.1: Schematic representation of an electrochemical cell.

2.2 Electrode materials

LiBs with graphite as a negative electrode have a theoretical capacity of 372 $\mathrm{mAhg^{-1}}$, whereas pure Si offers a theoretical capacity of 3580 $\mathrm{mAhg^{-1}}$. However, the practical application of pure Si as a negative electrode is severely limited due to its large volume expansion of up to 300% during charging. This expansion weakens the adhesion between the active material and the current collector, causing capacity loss and poor cycling performance. In addition, repeated breaking and reformation of the SEI consumes Li-ions, further reducing capacity. The significant volume changes also degrade the rate performance, as the thickening SEI hinders lithium-ion transport to the Si particles [7].

To overcome these issues, silicon oxide (SiO_x, $0 < x < 2$) is used as an alternative negative electrode material. The reduced volume expansion (150–200%) improves cycle life, enhances rate performance, and increases energy density compared to pure graphite. Nevertheless, challenges remain, including degraded cycling performance, formation of irreversible lithium silicate (Li_xSiO_y) and Li_2O during charging in the presence of oxygen, and capacity loss of 30–50% for SiO. Blending SiO_x with graphite in low mass ratios allows for incorporation of more active material while mitigating these issues [7].

In electrochemical curves (potential vs. state of lithiation), graphite exhibits steep slopes, whereas SiO_x shows a more gradual slope with stagnation, as illustrated in Figure 2.2. Charging corresponds to lithiation of the negative electrode and delithiation of the positive electrode [8].

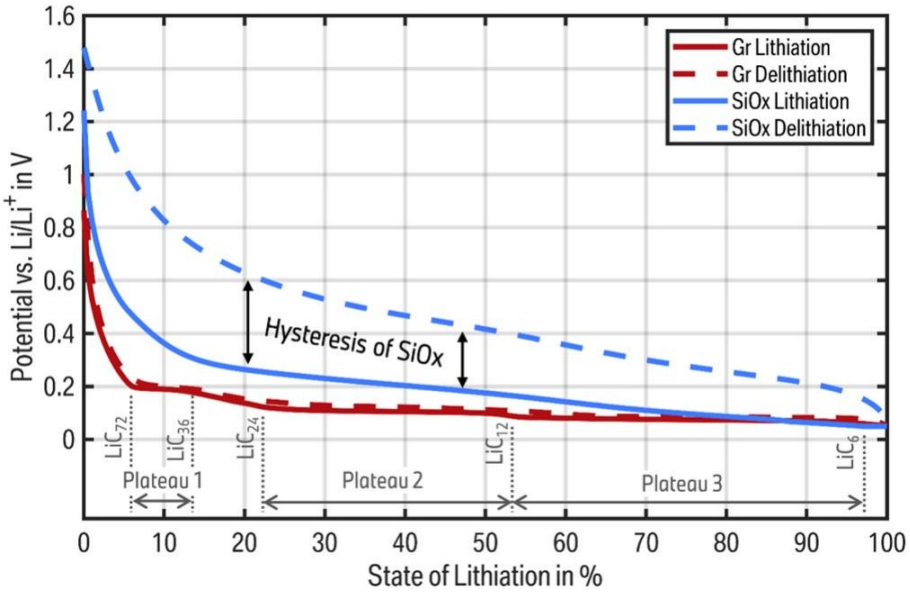

Figure 2.2: The overall increased potential and the hysteresis of SiO_x compared to graphite. Graphite phase transitions are associated with the graphite plateaus [8].

SEM images show that graphite particles exhibit a larger, flake-like morphology, whereas SiO_x particles are smaller and more irregular, distributed between graphite flakes [9]. In the cited example, graphite particles range from 9 to 15 µm, while SiO_x particles are approximately 7 µm, as shown in Figure 2.3. The images (a)–(c) highlight these differences in morphology.

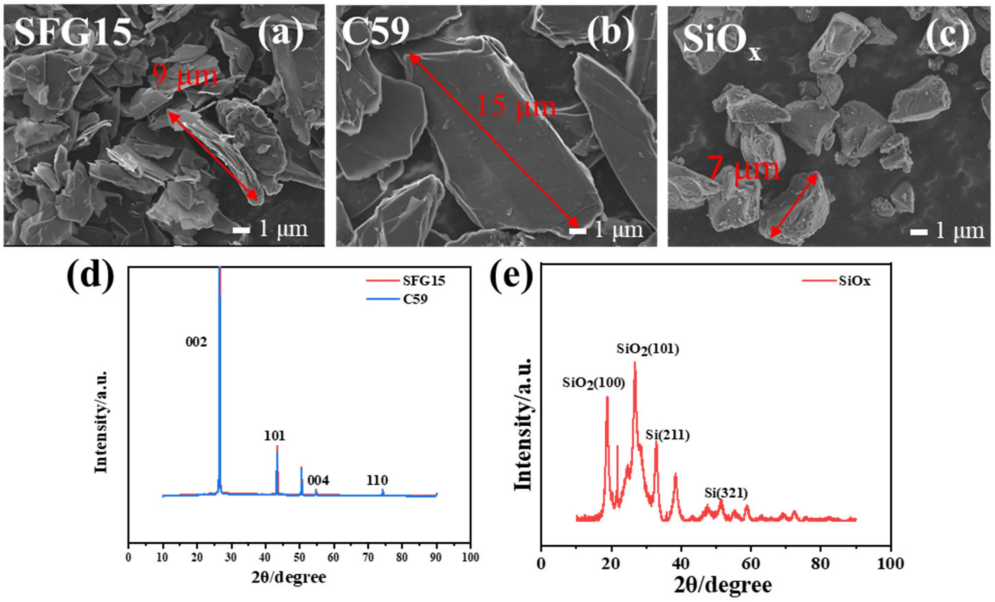

Figure 2.3: SEM images of two different graphites (a) and (b); SiO_x (c) [10].

2.2.1 Thermodynamics

The thermodynamic and kinetic properties of electrochemical reactions determine key battery performance parameters such as voltage, capacity, energy, and power. Thermodynamics defines the maximum achievable cell voltage and equilibrium behaviour, while kinetics governs the rate of electrochemical processes through mass transport and charge transfer limitations. The theoretical cell voltage, or electrochemical force (E_{cell}), is related to the Gibbs free energy change (ΔG_{cell}) by

$$\Delta G_{cell} = -nFE_{cell} \tag{2.1}$$

where F is the Faraday constant ($96\,485\,\mathrm{Asmol}^{-1}$) and n is the number of electrons transferred. The cell voltage is given by the difference between the electrode potentials:

$$E_{cell} = E_{positive} - E_{negative} \tag{2.2}$$

Under open-circuit conditions, the cell is in electrochemical equilibrium. During discharge, a spontaneous reaction occurs ($\Delta G_{cell} < 0$, $E_{cell} > 0$), while charging requires external energy to drive a non-spontaneous reaction ($\Delta G_{cell} > 0$, $E_{cell} < 0$) [11].

Under non-standard conditions, the cell voltage is described by the Nernst equation:

$$E_{cell} = E^0 - \frac{RT}{nF} \ln\left(\frac{a_+}{a_-}\right) \tag{2.3}$$

where R is the gas constant, T the temperature, and a_+ and a_- the activities of the oxidised and reduced species. For solids and electrons, the activity is typically assumed to be unity. Since absolute electrode potentials cannot be measured directly, the standard hydrogen electrode (SHE) is used as a reference, defined as 0 V. The Li/Li^+ couple has a standard potential of approximately $-3.045\,V$ versus SHE. For the LiB materials Li/Li^+ reaction is used as the reference [11].

2.3 Practical cell measures

The key properties relevant to the practical performance of an electrochemical cell under load conditions are the cell voltage, the cell capacity, and the efficient utilisation of energy and power. In the context of electric vehicles, the energy content of the cell corresponds to the driving range, while the power output determines the vehicle's acceleration capabilities [4].

The open-circuit voltage (OCV), measured under no-load conditions when no current flows, closely reflects the theoretical cell voltage. In Li-ion cells, the typical operating voltage ranges from approximately 3 V to 4.2 V. However, during operation the cell voltage deviates from the OCV due to internal losses [12]. When discharging, chemical energy is converted into electrical energy, with voltage reductions resulting from overvoltage or various forms of polarisation: activation (η_{ct}), concentration (η_c), and ohmic [13]. Activation polarisation results from charge transfer, whereas

concentration polarisation occurs due to mass transport limitations. Ohmic polarisation, known as internal resistance (IR drop), is typically the most significant source of voltage loss. The practical cell voltage can thus be described as:

$$E_{cell} = E_{pos} - E_{neg} - [\eta_{ct} + \eta_c]_{pos} - [\eta_{ct} + \eta_c]_{neg} - IR_0 \tag{2.4}$$

where I is the current, and R_0 represents the internal resistance [4].

Because of kinetic limitations and diffusion processes of the active species, the charge state of an electrochemical cell does not exactly mirror its discharge state. In part, this is a consequence of side reactions, which cause a temporal delay between the internal chemical and electrochemical reactions and the externally applied load or charging conditions during cycling. This mismatch results in a measurable voltage difference between the charge and discharge curves, known as voltage hysteresis, which is typically observed in the discharge profile of the cell [12][13].

The capacity of a cell is calculated from measurement of constant current charge and discharge within as specified voltage interval according to:

$$Q = \int_0^t I \cdot dt \tag{2.5}$$

where Q denotes the capacity (Ah), I is the applied constant current, and Δt represents the duration of the charge or discharge process. Specifically, for charging, Δt corresponds to the time elapsed from the initial state to the point at which the cell reaches its maximum specified voltage; for discharging, it is measured from the maximum voltage point to the cut-off voltage [14].

In this thesis, disharge capacity throughput is defined as the cumulative capacity, representing the total amount of charge that has passed through the battery during charge and discharge over time [15]. It can be expressed as

$$Q_{TP} = \int_0^t |I(t)| \cdot dt \tag{2.6}$$

where $I(t)$ is the discharge current and t is time [16].

The full cycle equivalent (FCE) is used to convert partial charge and discharge events into an equivalent number of full charge–discharge cycles. It is defined as

$$FCE = \frac{Q_{TP}}{2 \cdot Q_N} \tag{2.7}$$

where Q_N is the nominal battery capacity [16][17].

The C-rate is a measure of the charge and discharge rate of a battery and represents the current applied relative to the cell's rated capacity. A 1C rate implies that the cell is charged or discharged at a current that would deliver its full capacity in one hour. For example, a cell with a capacity of 3 Ah operating at a 1C rate

would be discharged at 3 A in one hour. If the same cell is discharged at a 4C rate, the discharge current would be 12 A, completing the process in 15 min. In contrast, at a C/10 rate, the discharge current would be 0.3 A, resulting in a discharge time of 10 h. Consequently, the discharge time is inversely proportional to the C-rate, and the applied current is equal to the product of the C-rate and the rated capacity [18]. The C-rate can be mathematically described as

$$C\text{-rate} = \frac{I}{Q_N} \tag{2.8}$$

where I is the charge or discharge current and Q_N is the nominal capacity of the battery [16].

The state of charge (SOC) indicates the ratio of the current charge level, $Q(t)$, to the available capacity, Q_n, expressed as a percentage:

$$SOC(t) = \frac{Q(t)}{Q_n} \cdot 100 \tag{2.9}$$

In LiBs, 100% SOC (fully charged) corresponds to all cyclable lithium ions residing in the negative electrode, while 0% SOC (fully discharged) indicates their presence in the positive electrode. Cell voltage decreases with decreasing SOC [19][20].

The rated capacity at beginning of life (BOL) serves as a reference point for evaluating capacity fade. Capacity measured at each cycle is normalised against BOL to monitor degradation over time. End of life (EOL) is reached when capacity falls below application requirements. Depth of discharge (DOD), defined as $DOD = 100\% - SOC$, quantifies the charge removed from a fully charged cell [4].

2.3.1 The cylindrical lithium ion cell

In a cylindrical Li-ion cell, the positive and negative electrodes are separated by a porous separator, with a tab attached to each electrode via ultrasonic or laser welding. These tabs, which are thin strips of conductive material, serve as connection points for the external circuit. The electrodes and separator are layered and then rolled into a cylindrical jellyroll, which is inserted into a metal casing. The negative electrode tab is welded to the base of the casing, forming the negative terminal, while the positive electrode tab is welded to the cap, which functions as the positive terminal. The cap is designed with a vent disc, which acts as a pressure relief mechanism to dissipate heat and gases in the event of overpressure within the cell. After assembly, the cell is filled with electrolyte, sealed by a crimping process, and finally enclosed in an external sleeve [21][22], as illustrated in Figure 2.4.

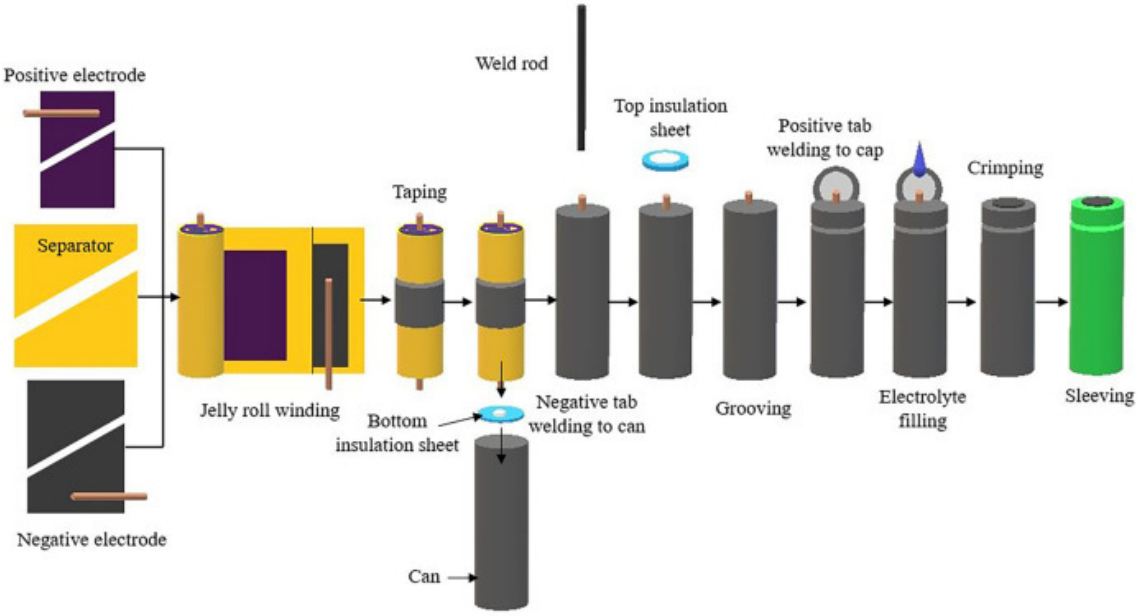

Figure 2.4: The process of a cylindrical LiB [21].

2.4 Ageing mechanisms

Battery degradation results from ageing of both active and inactive materials, causing performance decline. Chemical degradation appears as reduced capacity and power due to increasing internal resistance, impedance, and self-discharge rate. Mechanical degradation may disrupt electrical contact through separation of electrode material from the current collector or corrosion of inter-cell connections. These processes collectively lead to losses in battery performance: energy, power, and capacity [4]. The formation of the solid electrolyte interphase (SEI) and lithium plating are among the most commonly observed ageing mechanisms at the negative electrode. Particle cracking is most commonly seen on the positive electrode as a result from mechanical stress, where normal and shear stresses induce breakage or fracture of the active material [23].

2.4.1 Electrolyte stability

For chemical stability, the electrolyte must not be reduced at the negative electrode nor oxidised at the positive electrode. This thermodynamic stability is maintained when the Fermi levels of the electrodes align with the electrolyte's lowest unoccupied molecular orbital (LUMO) and highest occupied molecular orbital (HOMO), defining its electrochemical stability window (ESW). If the negative electrode's Fermi level exceeds the LUMO, reduction occurs; if the positive electrode's Fermi level falls below the HOMO, oxidation ensues. Thus, the open-circuit voltage (OCV) is limited by the ESW:

$$OCV = E_{Fneg} - E_{Fpos} \leq ESW \tag{2.10}$$

In practice, electrolytes are rarely stable across the full voltage range, leading to side reactions that form passivation layers on electrodes, which inhibit further de-

composition. In Li-ion cells at the negative electrode, this layer is known as the solid electrolyte interphase (SEI), which allows ion and electron transport under operating conditions [24].

The SEI forms on the surface of the negative electrode, acting as a passivating layer that prevents further electrolyte decomposition. Once formed, it adheres to the electrode and functions as an additional phase within the cell. The SEI inhibits electron transfer to the electrolyte while allowing lithium-ion transport. The SEI should ideally be thin, ionically conductive, and electronically insulating [25]. Its thickness, ranging from a few atomic layers to several tens of nanometres, depends on the electrode and electrolyte chemistries, and evolves with cell age and SOC [4].

2.4.2 Lithium plating

Lithium plating typically occurs during charging. Under conditions such as fast charging, low temperatures, or high SOC, the Li-ion concentration at the negative electrode increases, leading to overpotentials [26]. When the electrochemical potential of the graphite electrode drops below 0 V vs. Li/Li^+, lithium is deposited as metallic lithium onto the graphite surface instead of being intercalated into the graphite structure. Such conditions may arise even when the full cell voltage remains within its nominal operating window [27]. High upper cut-off voltages further promote lithium plating by increasing the SOC and associated overpotentials at the negative electrode [28]. A fraction of the plated lithium may be reintercalated during subsequent charging, while part of it reacts with the electrolyte to form additional SEI. The remaining plated lithium may become electrically isolated and coated with an inactive SEI layer, leading to a reduction in cyclable lithium and overall cell capacity [26].

2.4.3 Core collapse

Core collapse, also known as jellyroll collapse, occurs when the void at the centre of the cell becomes filled, causing the innermost coils of the jellyroll to deform inward. This deformation results from the repeated intercalation and de-intercalation of lithium ions into the electrodes, leading to expansion and contraction of the electrode materials. The resulting mechanical stress can cause delamination of the electrode coating from the current collector, thereby reducing the cell capacity. The expansion and contraction are often more pronounced in the negative electrode. Graphite can expand by approximately 10% during lithiation, while silicon forms alloys with lithium that may result in volumetric expansion of up to approximately 300%. In severe cases, such deformation may damage the separator and cause internal short circuits, potentially leading to thermal runaway [21].

2.5 Electrochemical methods

2.5.1 Electrochemical impedance spectroscopy

Electrochemical impedance spectroscopy (EIS) is a key technique for analysing electrochemical processes by measuring a cell's electrical impedance (Z) across a broad frequency range, typically from MHz to mHz. A sinusoidal voltage is applied under open-circuit conditions, and the resulting current is recorded, allowing analysis of phase shift and amplitude. EIS provides insights into mass transport, double-layer capacitance, and ohmic resistance. The applied potential and the resulting current can be described as follows:

$$E_{cell} = E_0 \sin(\omega t) \tag{2.11}$$

$$I = I_0 \sin(\omega t + \phi) \tag{2.12}$$

The impedance as a function of frequency is expressed by:

$$Z(\omega) = \frac{E}{I} = Z_0 \exp(j\phi) = Z_0(\cos\phi + j\sin\phi) \tag{2.13}$$

[29].

The resulting impedance $Z(\omega)$ is commonly visualised in a Nyquist plot, as illustrated in Figure 2.5, where the high frequency point on the real axis represents the bulk electrolyte resistance, R_s, and the semicircle diameter reflects charge transfer resistance, R_{ct}. The combination $R_s + R_{ct}$ corresponds to the local minimum on the real axis. The frequency at the peak of the semicircle, ω_{max}, relates to double-layer capacitance C_{dl}:

$$\omega_{max} = \frac{1}{R_{ct}C_{dl}} \tag{2.14}$$

At low frequencies, a linear tail indicates diffusion-limited processes, described by the Warburg impedance, W. The EIS can be used to track the battery ageing by analysing the changes seen in the Nyquist plot. A shift in the curve to the right shows an increased internal resistance. Thus, EIS serves as a valuable diagnostic tool for characterising cell performance and ageing [30].

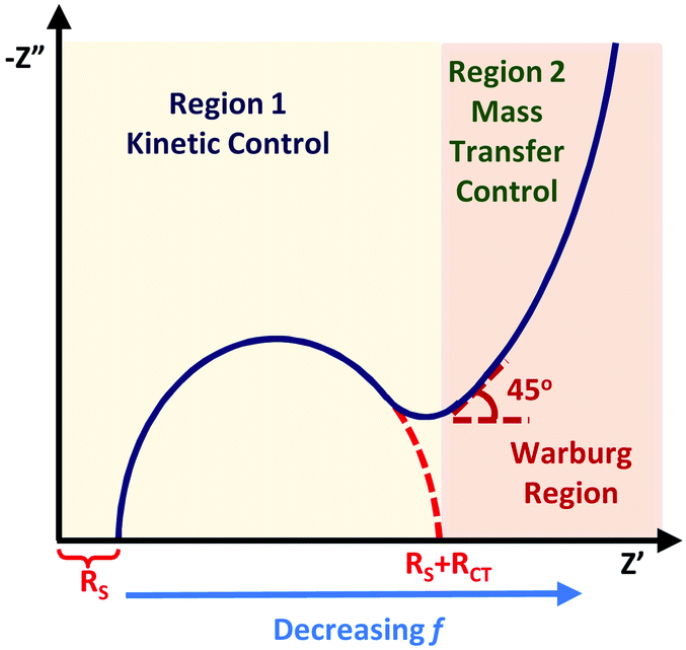

Figure 2.5: Nyquist plot [30].

2.5.2 Intermittent current interruption

The intermittent current interruption (ICI) technique is used to determine a battery's internal resistance (ohmic) and diffusion resistance. In this method, the cell is charged or discharged at constant current, followed by brief current interruptions (typically one to ten seconds). The resulting voltage response, an immediate voltage change, related to ohmic resistance, followed by a slower variation, provides insights into internal processes. The potential change in porous electrodes follows Fick's law and the de Levie transmission line model:

$$\Delta E(t) = \Delta E(0) - I \cdot k \cdot \sqrt{t} \tag{2.15}$$

where k is the diffusion resistance coefficient, determined from dividing the slope of the linear regression of potential versus $\sqrt{t}$ by the applied current:

$$k = -\frac{1}{I} \cdot \frac{d\Delta E}{d\sqrt{t}} \tag{2.16}$$

This coefficient is related to the diffusion coefficient σ, which can also be derived from the Warburg diffusion impedance in EIS [31][32].

$$k = \sigma\sqrt{8/\pi} \tag{2.17}$$

2.5.3 Incremental capacity analysis

Incremental capacity analysis (ICA) is a diagnostic method used to evaluate changes in a cell's electrochemical behaviour by calculating the differential capacity ($\Delta Q/\Delta V$) from variations in the voltage profile during cycling. Plateaus in the voltage profile, corresponding to phase equilibria, result in ICA becoming undefined at $\Delta V = 0$. The shape, width, amplitude, and position of the ICA peaks provide insight into active material utilisation and degradation processes within the cell. Broad peaks are generally associated with slower kinetics, increased heterogeneity, or structural changes, whereas peak shifts often indicate increased internal resistance, impedance growth, or enhanced polarisation. Reduced peak intensity may indicate loss of active material or cyclable lithium. The charge ICA profiles correspond to delithiation, whereas the discharge profiles correspond to lithiation. Although the charge and discharge profiles generally mirror each other, ageing increases the asymmetry between them due to hysteresis, polarisation, kinetic limitations, and diffusion related overpotentials. Consequently, changes in peak intensity, position, and shape provide insight into the underlying degradation mechanisms [4][33][34].

2.6 Lifetime testing

Lifetime testing is employed to evaluate the operational longevity and degradation behaviours of lithium ion batteries under controlled conditions [35]. Two principal types of accelerated lifetime tests are commonly used: calendar ageing tests and cycling ageing tests. Calendar ageing refers to battery degradation that occurs while the cell is at rest (standby mode), and is primarily influenced by two stress factors: temperature and SOC. In contrast, cycling ageing results from charge and discharge activity under various operational conditions. The four main stress factors in cycling tests are temperature, SOC, cycle depth, and C-rate [36]. To monitor battery performance over time, a reference performance test (RPT) should be conducted at regular intervals throughout the testing period [35].

2.6.1 Reference performance test

An RPT consists of a series of characterisation procedures designed to determine key performance parameters, such as capacity and internal resistance. Although there is no universally standardised RPT protocol, the specific procedures are typically tailored to suit the objectives of the study and the capabilities of the available testing facilities [35].

2.6.2 Load pattern

During accelerated cycling lifetime tests, different load patterns may be applied, depending on the test objectives. Common approaches include constant current–constant voltage (CCCV) charging and pulsed current profiles at various frequencies [36].

2.7 Non-destructive examinations

Non-destructive examination techniques are used to analyse the internal structure and morphology of battery cells without disassembly.

2.7.1 Computed tomography scanner

In computed tomography (CT), the battery is placed on a rotating stage and irradiated by an X-ray beam with initial intensity In_0. As the beam passes through the sample, it is attenuated according to the Beer–Lambert law:

$$In = In_0 \cdot e^{-\int \mu(x)\, dx} \tag{2.18}$$

where x is the thickness of the material (the length of the photon's path through the sample) and μ is the linear attenuation coefficient, which depends on the material properties and photon energy, and the integral represents the attenuation along the beam path. By measuring the transmitted intensity from multiple angles, the projection data can be expressed as

$$\ln\left(\frac{In_0}{I}\right) = \int \mu(x)\, dx \tag{2.19}$$

Reconstruction algorithms then use these projections to generate a three-dimensional attenuation map, $\mu(x, y, z)$, of the sample. For battery materials, the attenuation coefficient is primarily governed by photoelectric absorption, Compton scattering, and Rayleigh scattering:

$$\mu = \mu_{\text{photo}} + \mu_{\text{Compton}} + \mu_{\text{Rayleigh}} \tag{2.20}$$

Higher-energy processes such as pair and triplet production can be neglected, as they occur only above 1.022 MeV, which exceeds typical CT scan energies [37].

CT scanning can be used for macroscopic studies, such as evaluating electrode thickness, packing density, and layer alignment in assembled cells. It can also be applied at the microstructural level, enabling quantitative analysis of features such as particle size, tortuosity, and volume fraction [38]. In the present work, the analysis was limited to the macroscopic level. An example comparison from the literature between a well-manufactured cell and a flawed cell is shown in Figure 2.6. The well-aligned cell, shown on the right, exhibits uniformly stacked electrode layers with sufficient negative electrode overhang, meaning that the negative electrode extends beyond the positive electrode. In contrast, the flawed cell on the left exhibits misaligned and uneven electrode layers, indicating poor manufacturing control. In addition, regions where the positive electrode extends beyond the negative electrode can be observed, representing a critical defect that may promote lithium plating and dendrite formation [39].

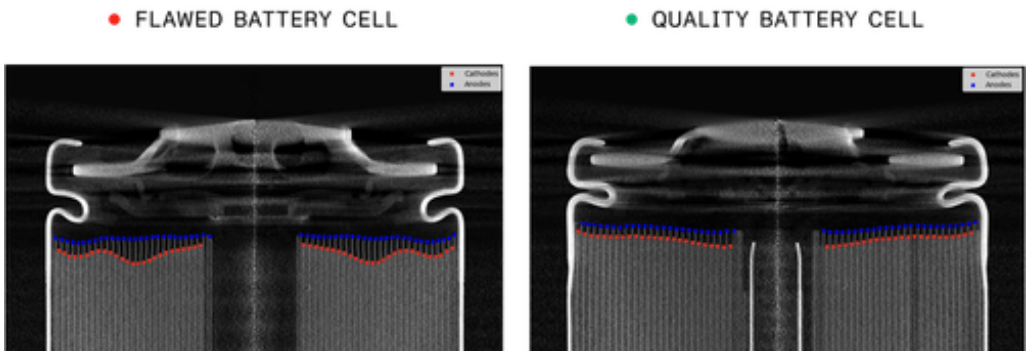

Figure 2.6: Literature example comparing a flawed cell (left) and a well-aligned cell (right), illustrating differences in electrode layer alignment and stacking quality [39].

2.7.2 Scanning electron microscopy and energy dispersive X-ray spectroscopy

Scanning electron microscopy (SEM) is a surface imaging technique with a resolution ranging from approximately 1 µm down to 1 nm, and magnifications up to 10^6. In SEM, a focused electron beam (typically 2–40 keV) is rastered across the sample surface. The interaction between the electrons and the sample generates a teardrop-shaped interaction volume, the size of which depends on beam energy, material composition, and incident angle [40]. Several signals are produced from these interactions, including secondary electrons (SE), backscattered electrons (BSE), and characteristic X-rays. SE are low-energy electrons emitted from near the surface and provide high-resolution topographical information. BSE originate from deeper regions and their intensity depends on atomic number, enabling compositional contrast. Characteristic X-rays are emitted when inner-shell vacancies are filled by outer-shell electrons, and their energies are specific to each element. These X-rays are detected using energy dispersive X-ray spectroscopy (EDX), which is commonly integrated with SEM to provide rapid qualitative and semi-quantitative elemental analysis of the sample [40]. The characteristic X-ray energies corresponding to each element are typically summarised in a periodic table chart [41].

2.8 3D printing

Three-dimensional (3D) structures can be designed using computer aided design (CAD) software and fabricated using additive manufacturing techniques. In this work, fused deposition modelling (FDM) was employed using an Original Prusa XL printer. In FDM, a thermoplastic filament is heated above its melting temperature and extruded through a nozzle to build the desired geometry layer by layer. The print head moves in the horizontal plane, while the build platform moves vertically to form successive layers. Polypropylene (PP) was selected due to its chemical resistance and suitability for laboratory environments. FDM enables fabrication of robust and functional components, such as the sample holders and adapters used in this work. However, PP may exhibit challenges such as warping during printing and relatively high material cost [42][43][44].

3
Methodology

Lifetime tests under various operating conditions were conducted to investigate cell ageing. The complete procedure for the assembly and testing of laboratory-scale cells is described in detail. To enable a comparative assessment between fresh and aged conditions, cell tear-down analyses were performed on one fresh cell and on selected aged cells from the lifetime testing programme. In addition, a dedicated tool for the teardown of cells with stainless steel casings was developed, designed, and manufactured.

3.1 Materials

For this master thesis, a commercial 18650 Li-ion cell, was selected. The specifications and key characteristics of the cell are presented in Table 3.1. The cell consists of a graphite negative electrode with a silicon oxide content of >10%, paired with a Lithium Nickel Manganese Cobalt Oxide (NMC) positive electrode. The dimensions of the cell are 65 mm in length and 18 mm in diameter.

Electrode materials recovered from disassembled commercial cells were used to assemble laboratory-scale cells. The electrodes are double coated; for assembly purposes, one side of each electrode was removed to expose the metal substrate (copper for the negative electrode and aluminium for the positive electrode). The electrolyte used in the laboratory-scale cells consisted of 1.2 M lithium hexafluorophosphate ($LiPF_6$) in a solvent mixture of ethylene carbonate (EC), ethyl methyl carbonate (EMC), and fluoroethylene carbonate (FEC) in a weight ratio of 27:63:10, supplemented with 2 wt.% vinylene carbonate (VC).

Table 3.1: Cell type and its characteristics.

Cell type	Capacity [mAh]	I [mA]	V_{min} [V]	V_{max} [V]
18650	4000	4000	2.5	4.2

3.2 Computed tomography scan

28 cells were sent to Volvo Cars for CT scanning. This enabled non-destructive examination of the internal cell structure prior to tear-down, even before conducting any electrochemical investigation. Using the associated software, key cell dimensions were measured. Figure 3.1a–Figure 3.1c present representative images of Cell 11, including dimensional measurements and cross-sections.

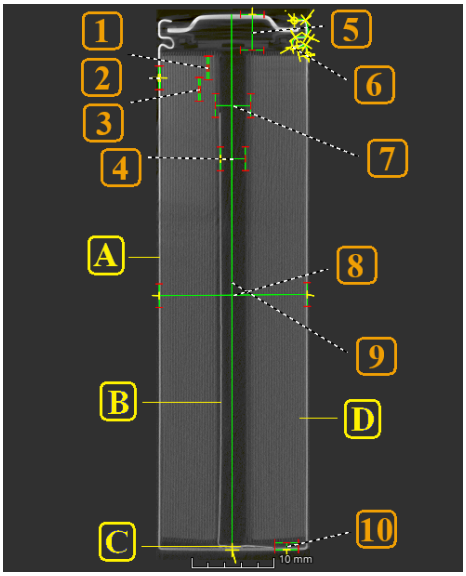

(a)

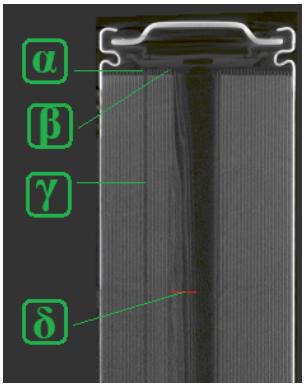

(b)

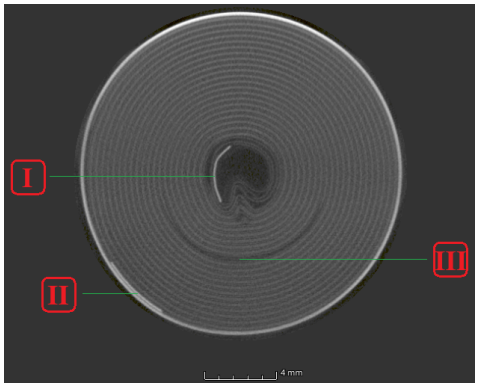

(c)

Figure 3.1: (a) Front view of the cell with the negative electrode predominantly visible and dimensional measurements indicated; (b) front view of the cell with the positive electrode predominantly visible; and (c) cross-sectional view of Cell 11.

A description of the figures above is presented in the following table.

Table 3.2: A description of Figure 3.1a-Figure 3.1c.

Index	Components	Measurement [mm]
1	Positive electrode	0.22
2	Casing thickness	0.22
3	Negative electrode	0.18
4	Centre free space	3.02
5	Cap height	4.31
6	Crimped length	9.36
7	Inactive material	4.28
8	Cell width	17.94
9	Cell length	64.91
10	Bottom free space	0.84
A	Casing	-
B	Negative electrode	-
C	Negative electrode welding	-
D	Positive electrode	-
α	Positive electrode tab	-
β	Negative electrode overhang	-
γ	Positive electrode	-
δ	Non-uniform winding and local electrode folding	-
I	Negative electrode tab	-
II	Negative electrode	-
III	Positive electrode tab	-

3.3 Full cell impedance analysis

The cells underwent impedance measurements using a Gamry 3000 instrument before cycling and after 300, 600, and 900 cycles, respectively. The frequency range was set from 0.1 to 200 kHz, and the perturbation voltage ± 1 V.

3.4 Lifetime testing setup

Initially, 5 test conditions with 3 test cells for each condition were designated. After 300 cycles, no distinct capacity degradation was observed. Consequently, two additional, more aggressive test conditions (11 and 12) were introduced, resulting in a total of 21 tested cells, see Table 3.3. Thermocouples were affixed to each cell to enable temperature monitoring during tests as a safety feature. Ensuring that any cell experiencing over temperature would be stopped, which were particularly important for test conditions 11 and 12.

All 21 cells were connected to individual channels within a custom rack configuration for the Neware BTS4000 instrument. For test conditions 1, 2, 3, 7, and 8, channels rated at 5 V and 6 A were sufficient, whereas test conditions 11 and 12 required channels rated at 5 V and 20 A. The Neware system was controlled via a

computer interface used to execute the test scripts.

3.4.1 Lifetime testing

The BTS 8.0.0 software was used to implement custom testing protocols via programmable scripts tailored to each test condition. For all test configurations, constant current constant voltage (CCCV) charging was applied with a cut-off current of 0.4 A (0.1C). For test conditions 1–8, the discharge current was maintained at 4 A (1C), whereas for test conditions 11 and 12 it was increased to 12 A (3C). Test conditions 1–3 employed a narrower voltage window, with a minimum of 3.046 V and a maximum of 4.06 V, corresponding to a voltage window of 60%. Test conditions 7 and 8 used a wider voltage window, resulting in a voltage window of 80%, while test condition 11 utilised the full voltage window. Nevertheless, for test condition 11 the cell is cycled between 4.2 to 2.5 V, however, due to the high current and IR drop, this results in 100% of the voltage window. The specific current and voltage parameters are summarised in Table 3.3.

Each RPT consisted of a capacity test, a series of pulses for impedance measurements, and an ICI test. During the RPTs, the full voltage window was applied, with limits of 2.5 V and 4.2 V. The charge and discharge currents during the capacity measurements were set to 1.2 A (0.3C) and 0.8 A (0.2C), respectively, with a cut-off current of 0.2 A (0.05C). During the HPPC test, the charge and discharge pulse currents were set to 4 A (1C), with pulse durations of 10 s followed by 40 s rest periods. The discharge current used to decrease the SOC from 100% to 80%, 50%, and 30% was 0.8 A (0.2C), with a 1 h rest period before the subsequent step. During the ICI measurements, the charge and discharge currents were set to 0.4 A (0.1C), with each step lasting 5 min followed by a 10 s pause. In total, each ICI measurement consisted of 117 charge steps and 117 discharge steps.

Table 3.3: Summary of conditions for the cell lifetime testing protocol.

Test condition	Cell ID	Charge	Discharge	V_{max} [V]	V_{min} [V]	SOC window [%]	Cycles	Disch. Q_{TP} [Ah]
2	11, 12, 13	0.8C	1C	4.06	3.046	60	900	2160
7	14, 15, 16	0.8C	1C	4.2	3.046	80	600	1920
8	17, 18, 19	0.8C	1C	4.06	2.569	80	600	1920
3	20, 21, 22	1C	1C	4.06	3.046	60	900	2160
1	23, 24, 25	0.5C	1C	4.06	3.046	60	900	2160
11	05, 06, 07	1C	3C	4.2	2.5	100	300	1140
12	08, 09, 10	1C	3C	4.2	3.08	50	600	1200

Upon completion of each test, the resulting data were exported via BTSDA software as Excel files, which were subsequently imported into Python for further analysis. Data processing and visualisation were performed within the Miniconda and PyCharm environments, with relevant packages installed.

An overview of the lifetime testing workflow is presented in the flow chart in Figure 3.2. This setup enables monitoring of capacity degradation and internal resistance growth over time. The lifetime testing sequence begins with the BOL stage,

followed by an initial RPT, and then a load pattern consisting of 50 cycles according to the specified test conditions. This is followed by a capacity test and a subsequent 50 cycle load pattern. The sequence is repeated until 300, 600 or 900 cycles are completed, concluding with a final RPT at EOL.

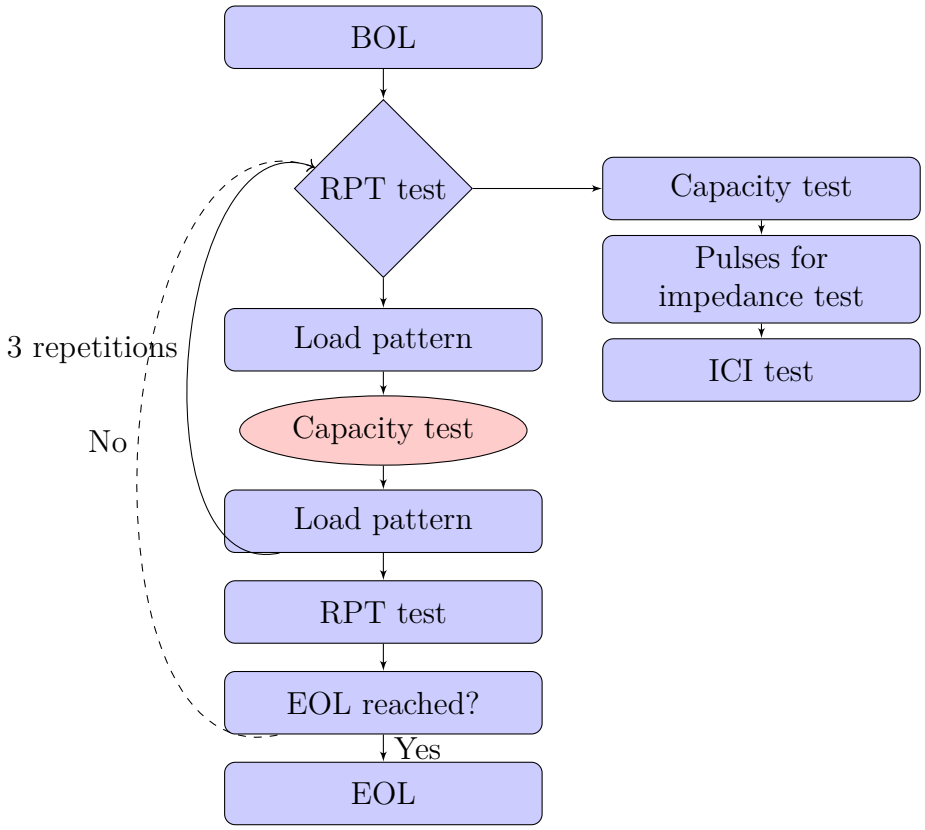

Figure 3.2: Flow chart illustrating the procedure for lifetime testing, including key stages such as BOL, RPT, load patterns, capacity assessments, and EOL evaluation.

3.5 Cell teardown

3.5.1 Traditional approach

A fresh cell (Cell 03) was selected for disassembly. Prior to disassembly, the cell was discharged to 0% SOC to minimise the risk of thermal runaway or electrical hazards in the event of a short circuit. The cell was not fully discharged to 0 V, but rather to 2.5 V, as the internal components were intended for reuse. The cell teardown was conducted in a controlled inert environment within a glovebox maintained at O_2, $H_2O < 1$ ppm. Appropriate personal protective equipment (PPE) was worn, including a laboratory coat and an initial pair of vinyl gloves. Upon inserting the hands into the glovebox, a second pair of vinyl gloves was donned, followed by a more durable pair for handling and opening the battery cells.

The first step in opening a cell was to use a pipe cutter to remove the lid. It is essential to make the incision where there is a gap between the jellyroll and the lid

to avoid damaging the internal components. The cutter, equipped with a sharp disc, was applied with light pressure against the battery casing. By gently rotating the cell, the stainless steel casing was gradually cut through, as illustrated in Figure 3.3a. Once the lid was removed, the connecting tab between the positive electrode and the lid was severed using ceramic scissors. To assist casing removal, a small portion of the lid was left attached, and the external plastic covering was removed beforehand. If the plastic covering was difficult to peel off, a ceramic knife or scissors could be used to create an opening. The stainless steel casing was then carefully peeled away using insulated flat pliers, exposing the jellyroll, as shown in Figure 3.3c. The jellyroll was subsequently unrolled for further analysis (Figure 3.3d). The region at the core of the jellyroll is referred to as the "inner" part, while the region at the beginning of the jellyroll before unfolding is referred to as the "outer" part. Both the inner and outer regions were sampled for SEM and laboratory-scale cell measurements. The fresh cell (Cell 03) was successfully disassembled using the traditional approach, although the procedure required considerable physical effort by Dr. Evelina Wikner. To simplify the disassembly of cells with stainless steel casings and reduce the required manual effort, a dedicated tool was subsequently developed.

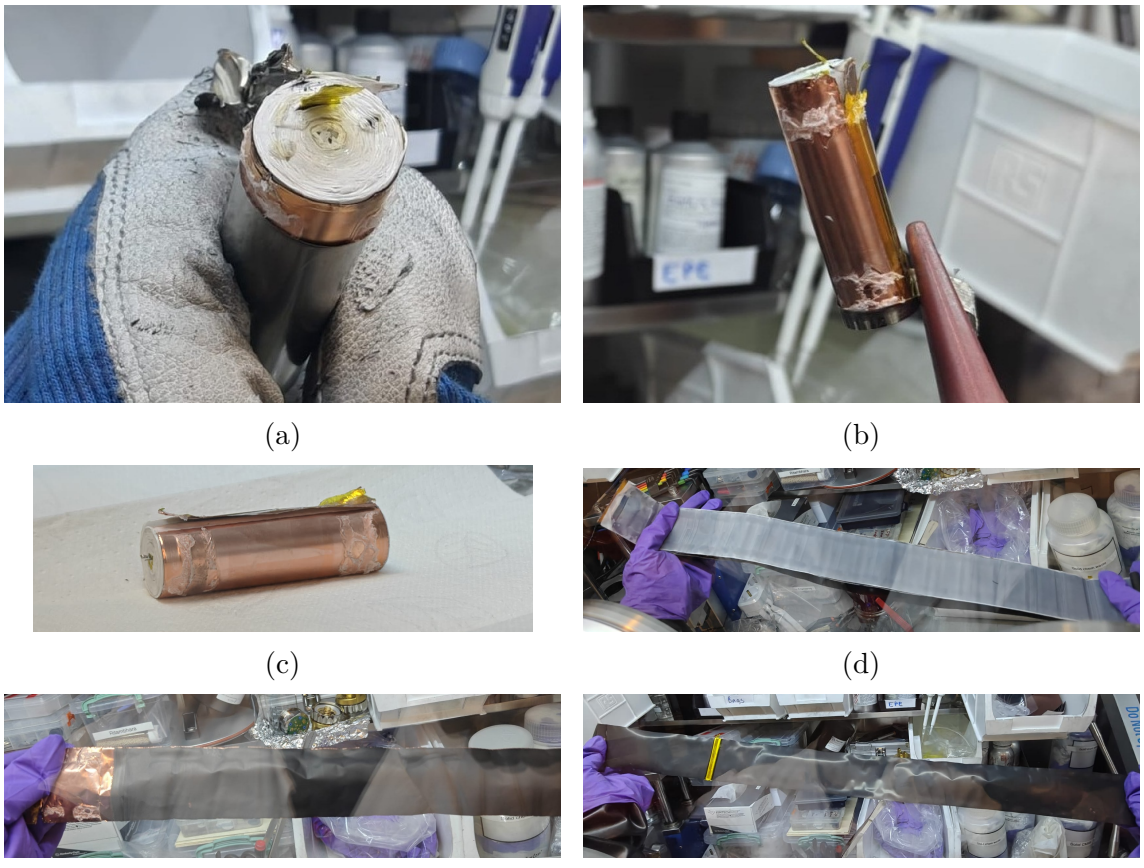

(a) (b) (c) (d) (e) (f)

Figure 3.3: Cell 03 disassembly: (a) peeling and (b) completion of peeling; (c) jellyroll and (d) unfolded jellyroll; (e) negative electrode and (f) positive electrode.

3.5.2 Design and production of the tool

The tool was developed to facilitate the disassembly of cells with stainless steel casings. The cell was positioned in a V-cut and secured by a sliding wall, enabling a rolling disc cutter to cut longitudinally along the cell length rather than circumferentially, as with a conventional pipe cutter. The cutter could also be adjusted vertically using a positioning table. The tool was designed in SolidWorks, and the final design is shown in Figure 3.4a and Figure 3.4b.

The V-cut block mounted on the base plate and the sliding wall were 3D-printed in polypropylene, while the remaining components were metallic. The 3D printer used was an Original Prusa XL, operated with the manufacturer's software, using design files exported from SolidWorks. The cutting disc and rails were made of stainless steel. The base plate, pillars, support brackets, and square holder (connecting the positioning table and guide blocks) were made of aluminium, whereas the disc holders were fabricated from galvanised steel. The base plate measured 26.5 cm in length and 19.1 cm in width, with a total tool height of 28 cm. A compact design was necessary to ensure placement within the glovebox. In addition, all sharp edges were polished to smooth surfaces to minimise the risk of puncturing the glovebox gloves. The tool accommodated cells with a maximum diameter of 26 mm and a maximum length of 80 mm. The tool was assembled by Dr. Douglas Nilsson Jutsell.

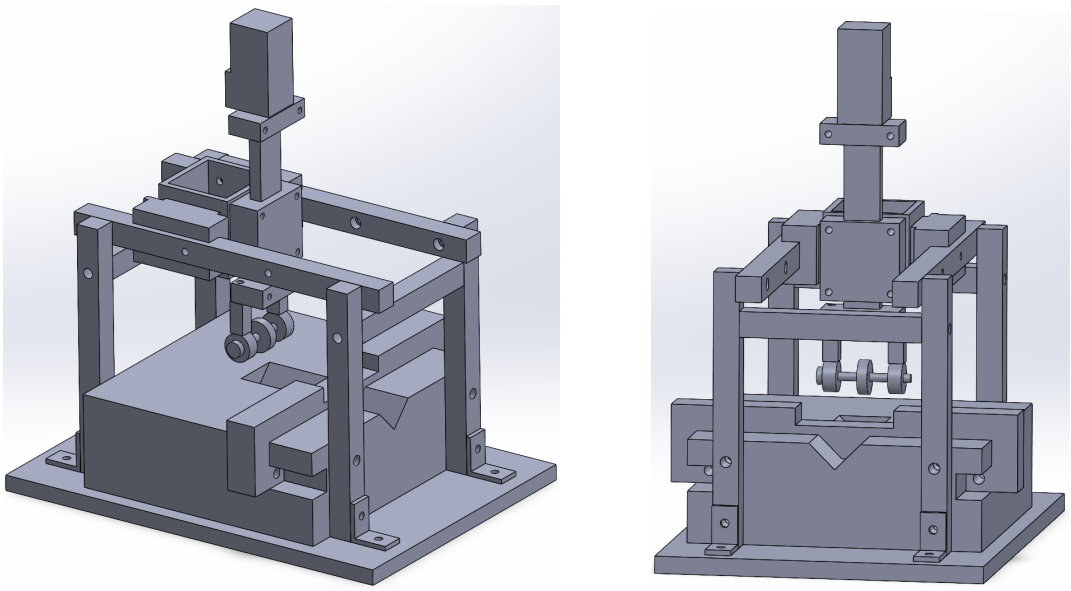

(a) (b)

Figure 3.4: Assembly of all parts in SolidWorks: (a) side view and (b) front view.

3.5.3 Cell tear down with in-house developed tool

Cycled cells 11, 15, and 19 were selected for teardown. Prior to disassembly, the cells were discharged to 2.5 V. The standard teardown protocol was then followed. The in-house developed tool was placed on a plastic mat inside the glovebox to electrically insulate it from the glovebox surface in the event of a short circuit. This precaution was necessary because the metallic cutting disc is mechanically connected to other metallic components, including the base plate. The cell was positioned in the V-cut and secured using the sliding wall (Figure 3.5a). The cap (positive terminal) was oriented towards the fixed wall of the V-cut, while the bottom (negative terminal) faced the sliding wall (Figure 3.5b). The cutter incorporates a mechanical stop that prevents the blade from contacting the cap, thereby reducing the risk of short circuit. In contrast, the sliding wall contains an opening that allows the cutter to pass beyond it, enabling cutting of the cell bottom.

When the cutter was at its highest position, the positioning table read 00.0 mm. Lowering the table to 13.0 mm cut through the outer plastic layer of the casing. As the stainless steel casing is approximately 0.2 mm thick, the blade was expected to reach full depth at 13.2 mm; however, in practice the cut remained superficial at this setting. The blade was therefore lowered incrementally by 0.1 mm at a time, rolling the disc from cap to bottom several times before further adjustment. Complete longitudinal cutting of the casing (Figure 3.5c) was achieved at a positioning table reading of 13.5 mm.

After cutting, the sliding wall was loosened and the cell was carefully removed from the tool. A small section at each end of the longitudinal cut was intentionally left attached and marked (Figure 3.5d). A pipe cutter was then applied just below the crimp of the cap to detach it, and the tab was severed using ceramic scissors (Figure 3.5e and Figure 3.5f). The remaining attached lid section was bent towards the longitudinal cut using insulated flat pliers. The pipe cutter was subsequently positioned as close as possible to the bottom of the cell to remove it completely, after which the tab was severed either with ceramic scissors or during removal of the bottom section (Figure 3.6a). Finally, the longitudinal cut was bent open using insulated flat pliers, allowing the jellyroll to be removed from the casing (Figure 3.6b–Figure 3.6d).

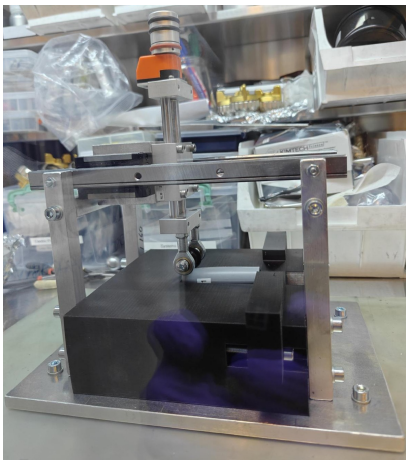

(a)

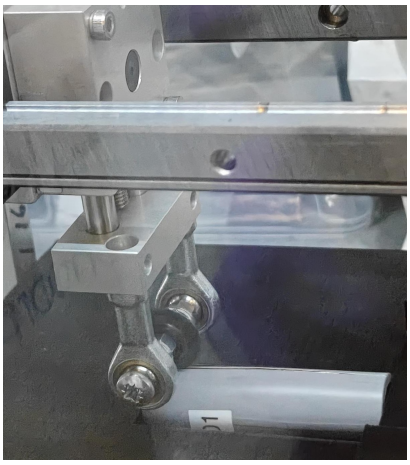

(b)

(c)

(d)

(e)

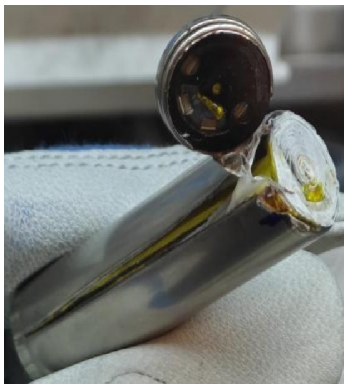

(f)

Figure 3.5: (a) Cell positioned in the V-cut of the in-house developed tool; (b) clean cut of the cell achieved using the tool. (c) Clean longitudinal cut of the cell using the in-house developed tool; (d) markings on the cap; (e) opened cap; (f) fully opened cap.

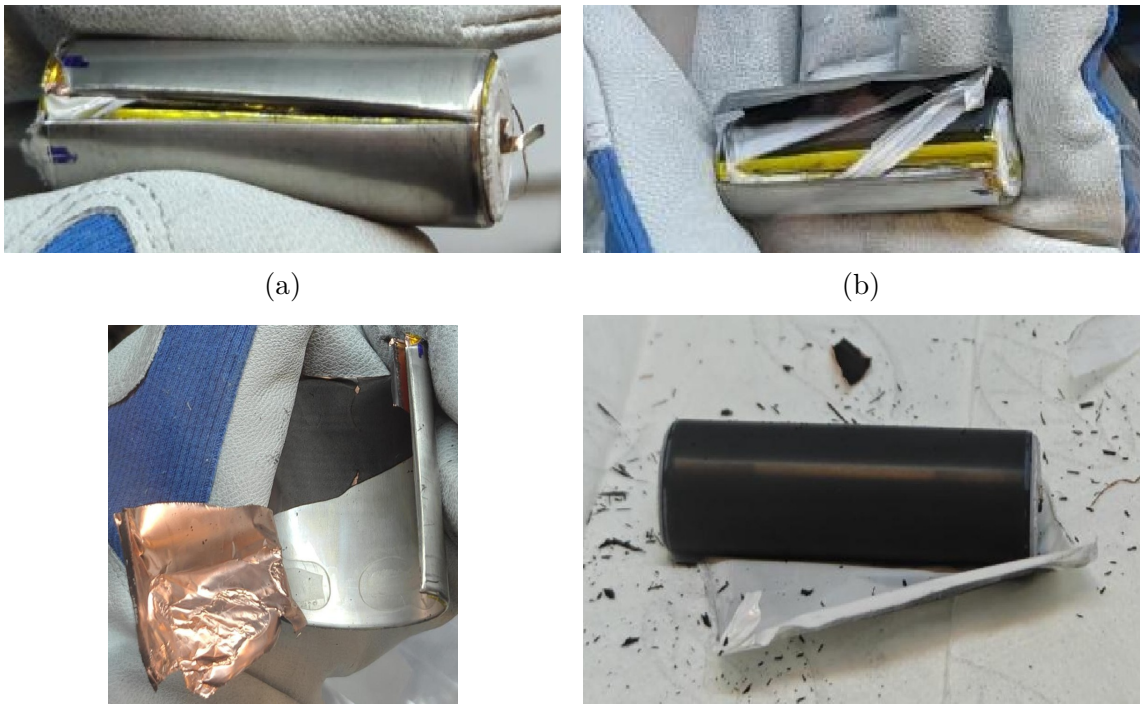

(a) (b)

(c) (d)

Figure 3.6: (a) Opened bottom section; (b) fully opened cell; (c) adhesive on the casing; (d) extracted jellyroll.

3.6 Preparation of negative and positive electrodes

Both the negative and positive electrodes are coated on both sides. For measurement purposes, one side of each electrode must retain the active coating (black), while the opposite side requires exposure of the underlying metal substrate, copper for the negative electrode and aluminium for the positive electrode. Therefore, it was necessary to remove the coating from one side of both the negative and positive electrodes, which can be seen in Figure 3.7a and Figure 3.7b. Fine-grained sandpaper was employed and carefully rubbed until small areas of the underlying metal surface became visible. Following this, the electrode was treated with 99.9% ethanol and gently wiped using cotton swabs to clean the surface. A minimum exposed surface area of approximately 4 cm in length by 2 cm in width was required to enable the punching of two discs with a diameter of 1.8 cm.

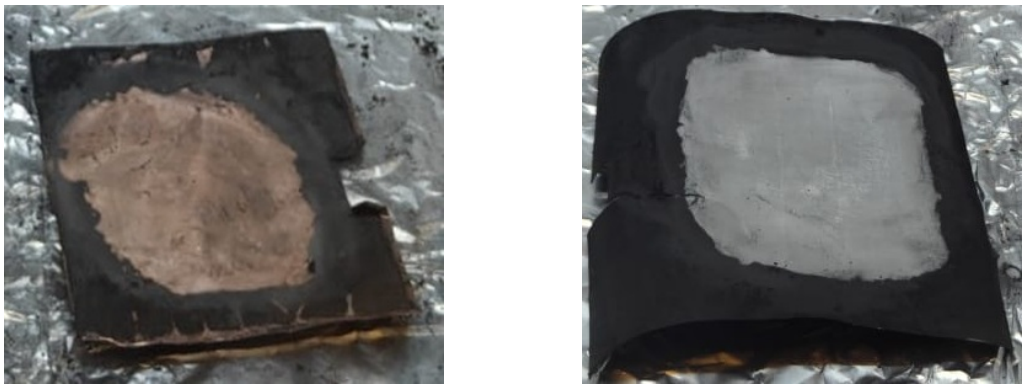

(a) (b)

Figure 3.7: (a) Negative copper electrode after polishing. (b) Positive aluminium electrode after polishing.

3.7 Scanning electron microscopy and energy dispersive X-ray spectroscopy

To ensure stable imaging conditions, the samples were prepared to be as conductive as possible by removing the electrode coating from one side of both the positive and negative electrodes, as described in the previous section. Five samples were prepared, representing the inner and outer regions of both electrodes (in addition, the middle region of the negative electrode for Cell 15), using a scalpel to cut. The samples were mounted on carbon tape attached to SEM stubs, which were then placed in an in-house developed SEM stub holder (Figure 3.8a). The SEM stubs were subsequently inserted into a Kammrath & Weiss GmbH portable transfer chamber, equipped with an electronically operated lid controlled by the corresponding transfer controller (Figure 3.8b). This procedure prevented exposure to air and maintained the samples in an argon atmosphere identical to that of the glovebox. The portable chamber was secured in a designated container for transport to the SEM facility (Figure 3.8c).

Imaging was performed using a GeminiSEM 450 (Gemini 2) from Zeiss, operated with the manufacturer's software. After purging the SEM chamber with nitrogen, the transfer chamber was mounted onto the SEM (Figure 3.8d). In this study, an accelerating voltage of 5 kV, a probe current of 250 pA, and a working distance of approximately 8.5 mm were used. Once a region of interest was identified, magnification, working distance, focus, and contrast were adjusted. The images presented in the results were acquired at a magnification of 5000×.

EDX analysis was performed using the AZtec software. To increase the count rate, the probe current was initially raised to 1 nA, but was later returned to 250 pA due to charging observed in the SEM images. All other parameters were kept identical to those used for SEM imaging. Elemental analysis was conducted on selected surface regions to determine the elements present and estimate their relative abundances.

Elemental mapping was subsequently performed to visualise the spatial distribution of the detected elements across the analysed area. SEM and EDX data collection was conducted by Dr. Ritambhara Gond.

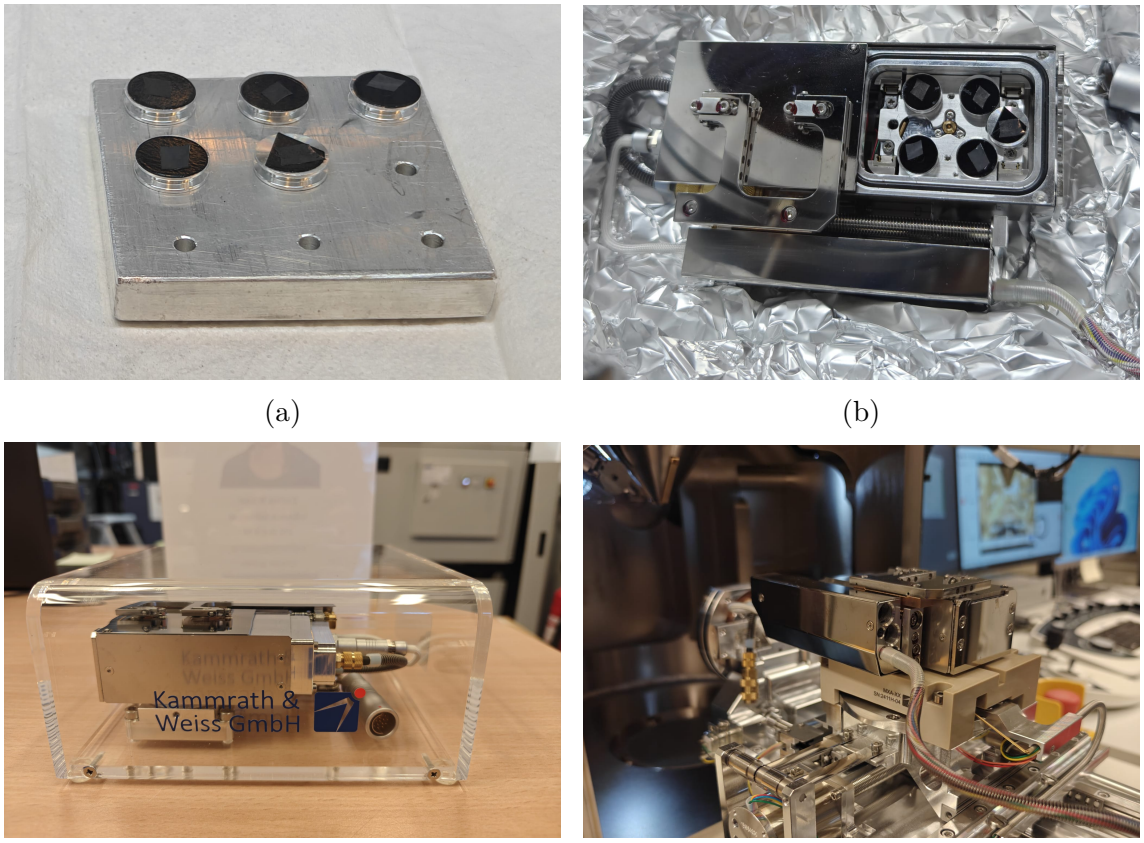

(a) (b)

(c) (d)

Figure 3.8: (a) SEM stubs mounted in an in-house developed holder; (b) samples in the portable transfer chamber, inside of the glovebox; (c) portable chamber secured in a container for transport; (d) transfer chamber mounted onto the SEM.

3.8 Laboratory cell assembling

Laboratory-scale cells, hereafter referred to as PAT-cells, were assembled using the previously punched electrode discs. For each electrode (inner and outer), two PAT-cells were assembled to provide replicates for consistency and to ensure at least one cell remained usable in case of measurement failure. For the positive half-cell configuration, the positive electrode was positioned with the aluminium (Al) current collector against the lower plunger, while lithium (Li) metal served as the negative electrode. In the negative half-cell configuration, the graphite electrode with the copper (Cu) current collector acted as the positive electrode, paired with lithium metal as the negative electrode. A separator was placed between the electrodes within an insulating sleeve. A schematic of the PAT-cell assembly is presented in Figure 3.9.

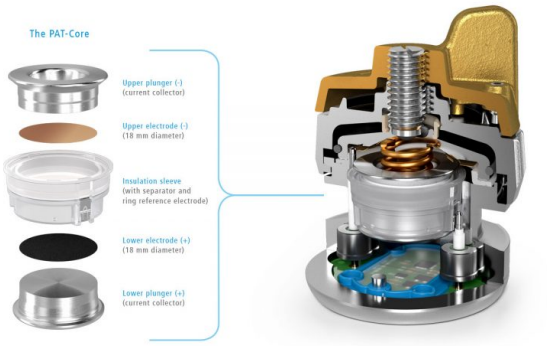

Figure 3.9: Schematic illustration of the PAT-core components (adapted from [45]).

The assembly of the PAT-cell was performed entirely within a glovebox due to the air sensitivity of the electrodes and the toxicity of the electrolyte. A polyethylene (PE) seal ring was placed inside the PAT-cell lid prior to assembly. All components required for assembling six PAT-cells are shown in Figure 3.10a. The assembly process began by positioning the insulation sleeve upside down. The positive electrode was then placed onto the separator using tweezers, ensuring that the black-coated side was in contact with the separator and that the current collector faced upwards. The lower plunger was subsequently placed onto the current collector, with the plunger facing downwards towards the base of the PAT-cell and the separator facing upwards. An alignment mark on the insulation sleeve was matched with the lower half of the PAT-cell to ensure correct orientation. Thereafter, 100 µL of electrolyte was dispensed onto the separator using a pipette, as illustrated in Figure 3.10b. The negative electrode was then carefully placed on top of the separator. Finally, the upper plunger was positioned onto the negative electrode, and the PAT-cell lid was secured by rotating it to lock the cell. In a half cell configuration the electrode material to be studied is the positive electrode, while the negative electrode is Li.

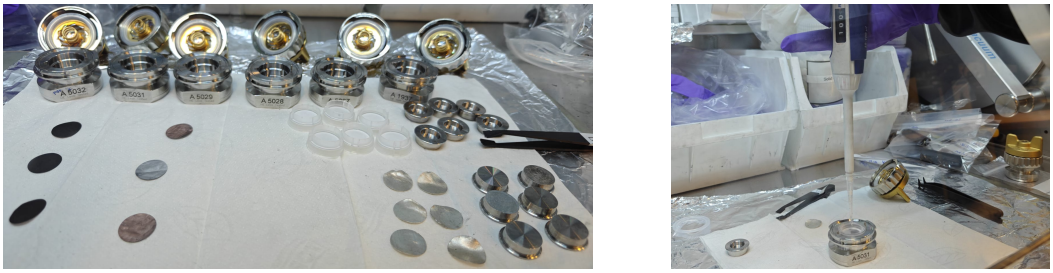

(a) (b)

Figure 3.10: (a) All components to assembly 6 PAT-cells. (b) 100 µL of electrolyte was dispensed onto the separator using a pipette.

3.9 Material characterisation of laboratory-scale cells

The EmStat4S setup is illustrated in Figure 3.11a. Custom scripts for capacity and impedance analyses were developed using PCTrace software for single device

operation and MultiTrace (Individual mode) for parallel measurements of up to 12 devices; in this thesis, 6 devices were operated simultaneously (depicted in Figure 3.11b). The resulting data were exported in CSV format and subsequently processed in Python for further analysis. The electrode connections were configured as follows: the reference electrode was connected to the blue lead, the working electrode to the red lead, the sense working electrode to the white lead, and the counter electrode to the black lead. The green lead corresponds to the ground electrode and was not used in this experiment. On the left side of the device are the current input terminals, where terminal 1 is positive and terminal 2 is negative. On the right side are the voltage input terminals: S1 corresponds to the positive electrode, R to the reference electrode, and S2 to the negative electrode.

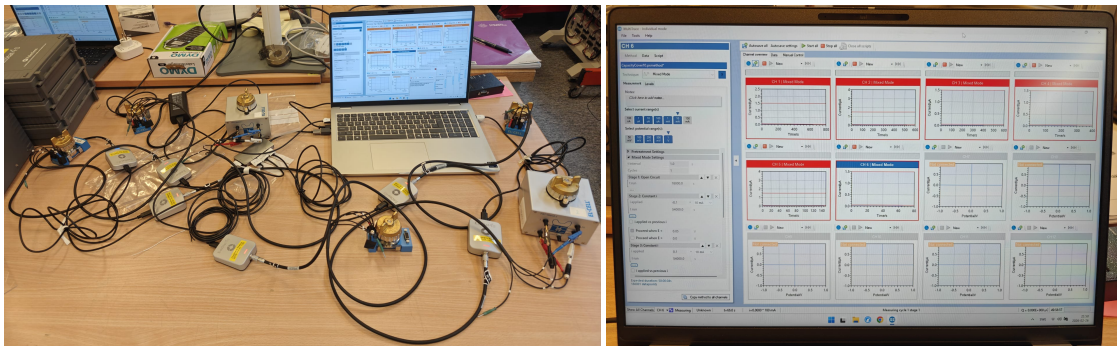

(a) (b)

Figure 3.11: (a) The EmStat4S setup. (b) 6 devices using MultiTrace software.

3.9.1 Capacity measurement

For all PAT-cells, the capacity was initially estimated at approximately 10 mAh, resulting in a C/10 current of 1.0 mA. Charge and discharge times were set to 15 h, with an additional 5 h margin to accommodate cells with higher than expected capacity. Voltage limits were set between 2.5 V and 4.2 V for positive electrodes, and between 0.05 V and 1.5 V for negative electrodes. Prior to measurement, freshly assembled PAT-cells were allowed to rest for 5 h to ensure electrode wetting.

3.9.2 Impedance analysis

Impedance analysis was performed using custom scripts in PCTrace or MultiTrace for the EmStat4S instrument following the capacity measurements. The applied current was adjusted according to the measured PAT-cell capacities. The procedure is summarised in the flow chart presented in Figure 3.12 and was designed to acquire impedance data at successive state-of-charge (SOC) intervals of 10%, from 0% to 100% SOC.

For positive electrodes, the PAT-cell was initially discharged to the minimum voltage limit of 2.5 V, and an EIS measurement was performed at 0% SOC. A current pulse was then applied up to the maximum voltage limit of 4.2 V. The SOC was subsequently increased in 10% increments, with a defined rest period prior to each

EIS measurement, until 80% SOC was reached. An additional step to 90% SOC was performed, followed by a rest period and an EIS measurement during which only a discharge pulse was applied. The analysis concluded at 100% SOC with a final EIS measurement. During EIS measurements, the frequency range was set from 0.1 Hz to 200 kHz, identical to the range used for the full cell.

For negative electrodes, the procedure was reversed: the PAT-cell was initially charged to the maximum voltage limit of 1.5 V, and the SOC was subsequently decreased in 10% increments to 0%, with rest periods and EIS measurements identical to those described for the positive electrodes. The pulse current for negative electrodes was applied down to the minimum voltage limit of 0.05 V.

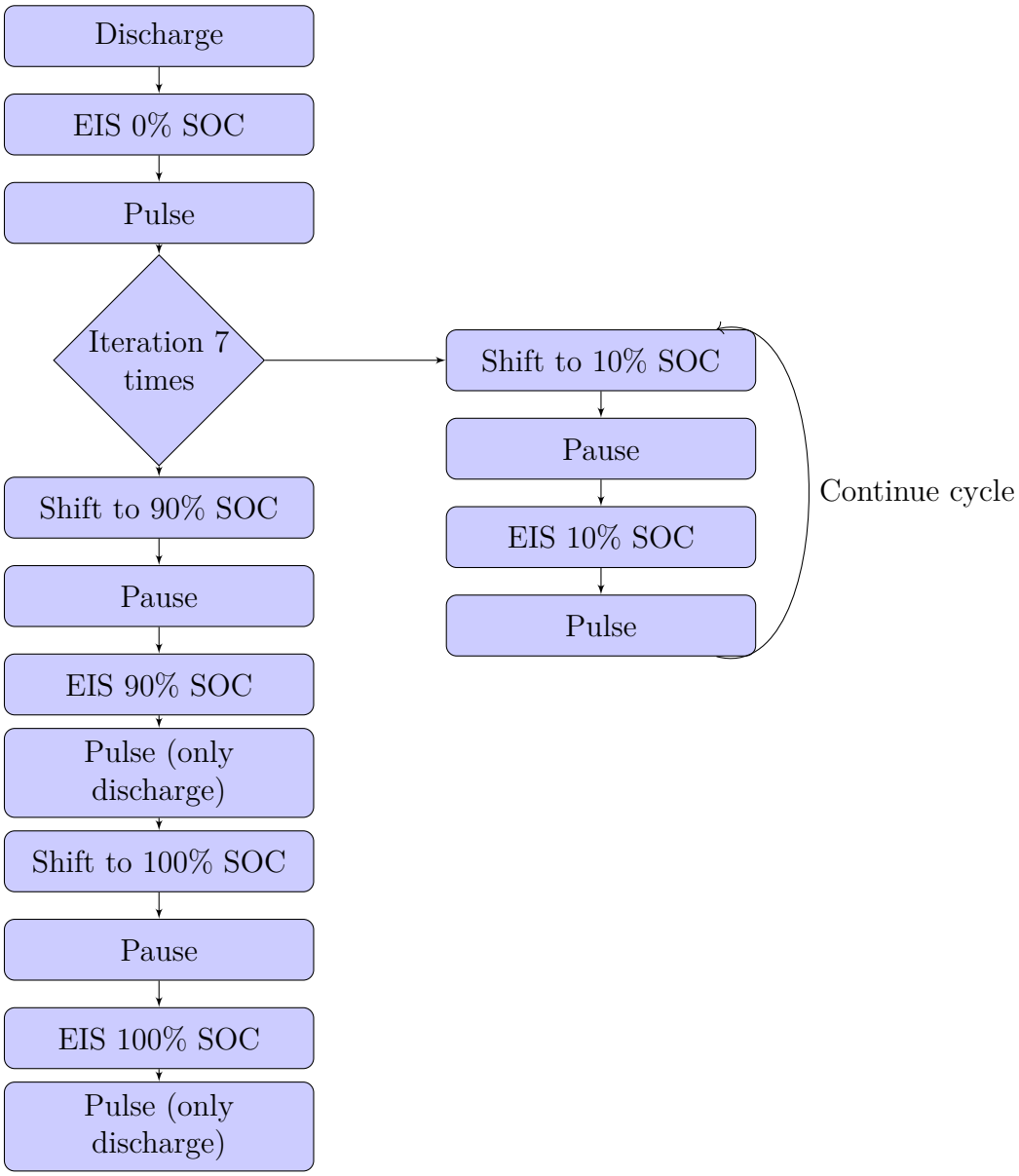

Figure 3.12: Flow chart illustrating the procedure for electrochemical impedance spectroscopy (EIS) and pulse testing.

4
Results

The results are organised according to the main objectives of the study. First, the lifetime testing results are presented, including capacity fade, impedance analysis, and ICA. This is followed by the CT analysis, which provided non-destructive information regarding the internal cell structure. Subsequently, the development of the in-house teardown tool and the findings from the cell teardown are described. Finally, the post-mortem analyses, including SEM, EDX, and electrochemical characterisation of PAT-cells, are presented. Except for the capacity fade and resistance growth results, the analyses primarily focus on the fresh reference cell (Cell 03) and three selected aged cells: Cell 11 from TC 2 (centred voltage window), Cell 15 from TC 7 (higher upper voltage limit), and Cell 19 from TC 8 (lower voltage limit). These cells were selected to represent different ageing behaviours associated with the investigated cycling conditions. Detailed information regarding the applied test conditions is provided in Table 3.3, which is referred to frequently throughout this chapter.

4.1 Lifetime testing

The Neware cycling protocol was divided into blocks of 300 cycles, each test spanned approximately 26 to 32 days. Consequently, depending on whether one, two, or three tests were conducted, the total experimental duration ranged from approximately 50 to 64 days or 75 to 94 days. The primary observable outcome of the lifetime testing was cell ageing, reflected by a decrease in capacity and an increase in impedance. A greater reduction in capacity or increase in impedance therefore indicates a more advanced state of ageing. Detailed information regarding the various test conditions is provided in Table 3.3.

4.1.1 Capacity fade

Capacity fade was calculated according to Equation 2.6. The evolution of capacity degradation is presented for TCs 1 (Cells 23–25), 2 (Cells 11–13), and 3 (Cells 20–22) in Figure 4.1c; for TCs 2 and 8 (Cells 17–19) in Figure 4.1a; for TCs 7 (Cells 14–16) and 8 in Figure 4.1b; and for TCs 11 (Cells 5–7) and 12 (Cells 8–10) in Figure 4.1d. The corresponding BOL and EOL capacity values are summarised in Table 4.2. TCs 1, 2, and 3 employed a centred voltage window with the same voltage window width but different charge C-rates. TC 7 employed a higher upper voltage limit and a wider voltage window than TCs 1–3, whereas TC 8 employed a lower voltage limit while retaining the same voltage window width as TC 7. TCs 2, 7, and 8 were cycled at the same charge C-rate. TCs 11 and 12 employed a discharge C-rate three times higher than the remaining test conditions, while TC 11 additionally utilised the full voltage window range.

The capacity fade observed for TCs 1, 2, and 3 was relatively similar, with all cells retaining more than 90% of their initial capacity, as shown in Figure 4.1c. In contrast, clear differences were observed when comparing TCs 2 and 8, as well as TCs 7 and 8, as shown in Figure 4.1a and Figure 4.1b, respectively. Under test condition 8, the remaining capacity decreased substantially to approximately 35–40%, whereas the cells subjected to TCs 2 and 7 retained more than 90% of their initial capacity and exhibited similar degradation trends.

TCs 7 and 8 employed the same voltage window width. However, the voltage window placement differed. The lower voltage limit for TC 8 reached 2.569 V, compared with 3.046 V for TCs 2 and 7. In contrast, test condition 7 employed a higher upper voltage limit of 4.2 V, whereas test conditions 2 and 8 used an upper limit of 4.06 V. TCs 11 and 12 exhibited comparatively limited degradation, making it difficult to draw clear conclusions from these cycling conditions. Consequently, TCs 11 and 12 are not discussed further.

The temporary decrease in capacity and increase in resistance observed at approximately 800 Ah, followed by partial recovery around 1400 Ah, are attributed to relaxation effects occurring during the rest periods between 300, 600, and 900 cycles, as the Neware cycling protocol was divided into blocks of 300 cycles.

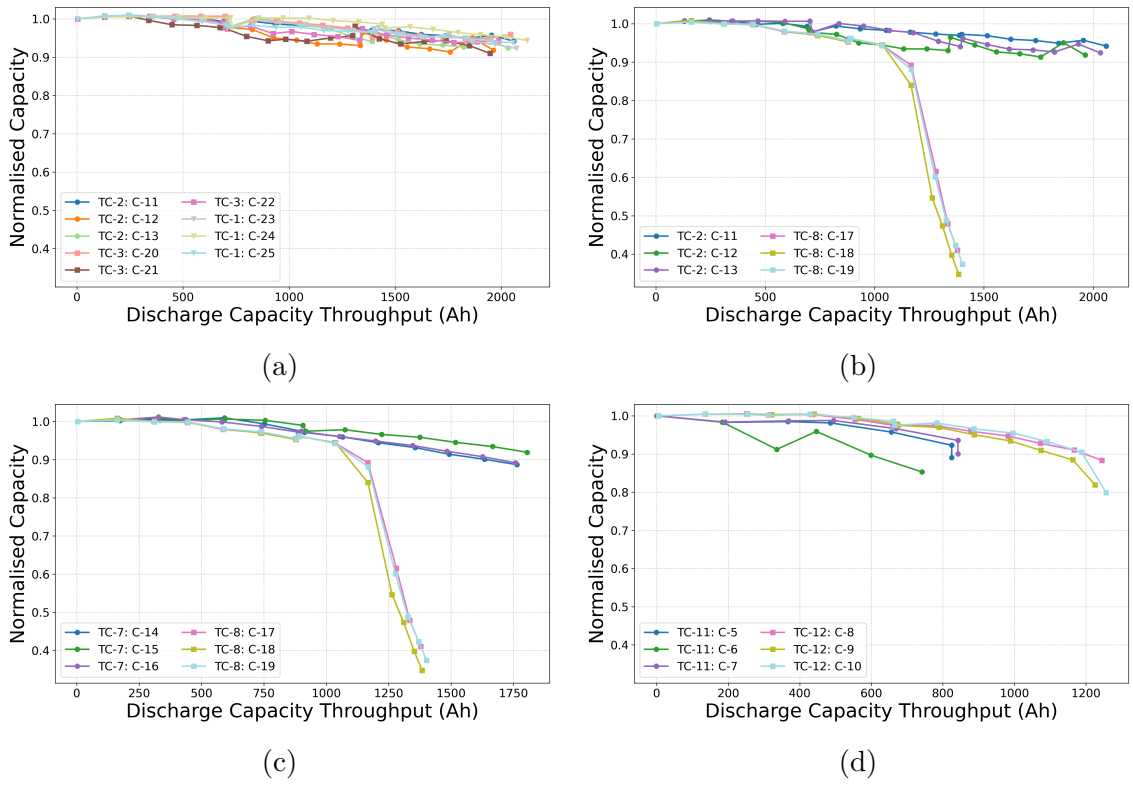

Figure 4.1: Normalised capacity as a function of discharge capacity throughput for different test conditions: (a) 2 and 8; (b) 7 and 8; (c) 1, 2, and 3; and (d) 11 and 12.

4.1.2 Impedance analysis

The other non-destructive examination presented in this study is the impedance analysis of the full cells. Nyquist plots of the fresh Cells 26, 27, 28, and 29, together with a comparison between the BOL of Cell 26 and the EOL of Cells 11 (TC 2, centred voltage window), 15 (TC 7, higher upper voltage limit), and 19 (TC 8, lower voltage limit), are presented in Figure 4.2a and Figure 4.2b, respectively. In the Nyquist plots, the high frequency intercept at the beginning of the semicircle corresponds to the ohmic resistance, R_s, while the width of the semicircle extending to the onset of the low frequency tail corresponds to the charge transfer resistance, R_{ct}. The values of R_s and R_{ct} for the BOL of Cells 26, 27, 28, and 29, as well as the EOL of Cells 11, 15, and 19, are summarised in Table 4.1. Further details regarding the ageing conditions applied to the respective cells are provided in Table 3.3.

Cells 26, 27, 28, and 29 were measured in the fresh state and used as BOL references for the aged cells, as their Nyquist plots overlap closely (Figure 4.2a). As shown in Figure 4.2b, the EOL cells, Cell 11 (remaining capacity of 96%, TC 2, centred voltage window), Cell 15 (92%, TC 7, higher upper voltage limit), and Cell 19 (37%, TC 8, lower voltage limit), all exhibited increased ohmic resistance, R_s, compared with the fresh reference cell. The increase was relatively small for Cells 11 and 15, whereas Cell 19 showed a substantially larger increase. In addition, the diame-

ter of the semicircle, corresponding to the charge transfer resistance, R_{ct}, increased significantly for all aged cells compared with the fresh reference cell, as summarised in Table 4.1. Cell 19, which exhibited the greatest capacity fade, also displayed the highest internal resistance. However, Cell 19 retained a distinct semicircular arc, whereas Cells 11 and 15 exhibited more depressed and flattened semicircles.

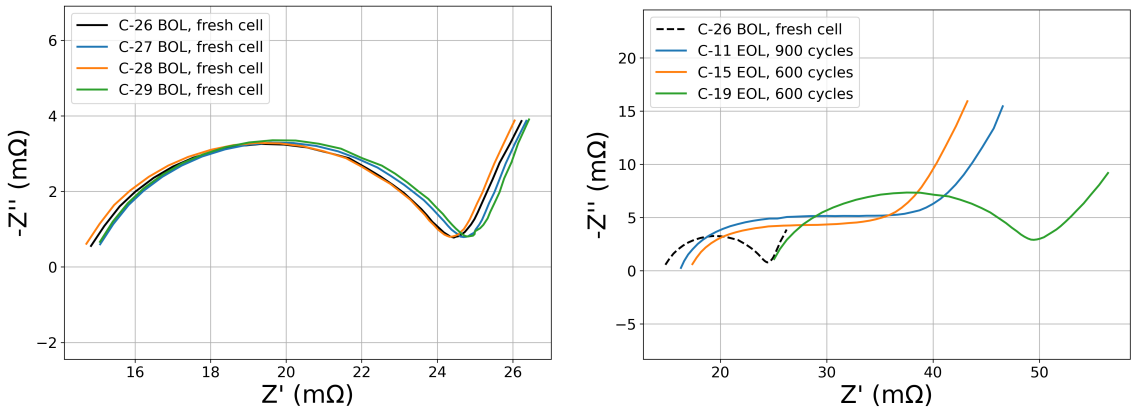

(a) (b)

Figure 4.2: EIS measurements of (a) fresh Cells 26, 27, 28, and 29, and (b) BOL Cell 26 compared with the EOL of Cells 11, 15, and 19.

Table 4.1: Ohmic and charge transfer resistance (R_s and R_{ct} of the cells at BOL and EOL.

Test condition	Cell ID	BOL/EOL	R_s [mΩ]	R_{ct} [mΩ]
Fresh cell	Cell 26	BOL	14.84	9.65
Fresh cell	Cell 27	BOL	15.08	9.74
Fresh cell	Cell 28	BOL	14.71	9.77
Fresh cell	Cell 29	BOL	15.07	9.74
2	Cell 11	EOL	16.30	22.43
7	Cell 15	EOL	17.37	18.50
8	Cell 19	EOL	25.06	24.40

The evolution of internal resistance at 50% SOC is presented for TCs 1, 2, and 3 (centred voltage window) in Figure 4.3a, for TCs 2 and 8 (lower voltage limit) in Figure 4.3b, for TCs 7 (higher upper voltage limit) and 8 in Figure 4.3c, and for TCs 11 and 12 (higher discharge C-rate) in Figure 4.3d. Internal resistance was determined from ICI measurements using high resolution time domain data. The resistance was calculated from the instantaneous voltage change upon current interruption using the ratio $\frac{\Delta V}{\Delta I}$ at the moment of the current step. The voltage difference was evaluated between the data points immediately before the current interruption and immediately before the current resumed, corresponding to a pause duration of 10 s. The resulting resistance therefore includes both the ohmic contribution and a contribution from charge transfer processes, as the voltage relaxation was evaluated over a 10 s interruption period. To reduce the runtime of the data processing scripts, the Excel files were converted to CSV format using Python. The values of R_{10s} at BOL and EOL for the respective cells are summarised in Table 4.2.

As shown in Figure 4.3b and Figure 4.3c, the cells subjected to TC 8 (lower voltage limit) exhibited a substantially larger increase in R_{10s} compared with TCs 2 and 7. Cell 18 showed the most pronounced resistance increase among all investigated cells. In contrast, the remaining test conditions followed comparatively similar trends, where the EOL R_{10s} values remained below approximately 1.5 times the corresponding BOL values, as shown in Figure 4.3a and Figure 4.3d.

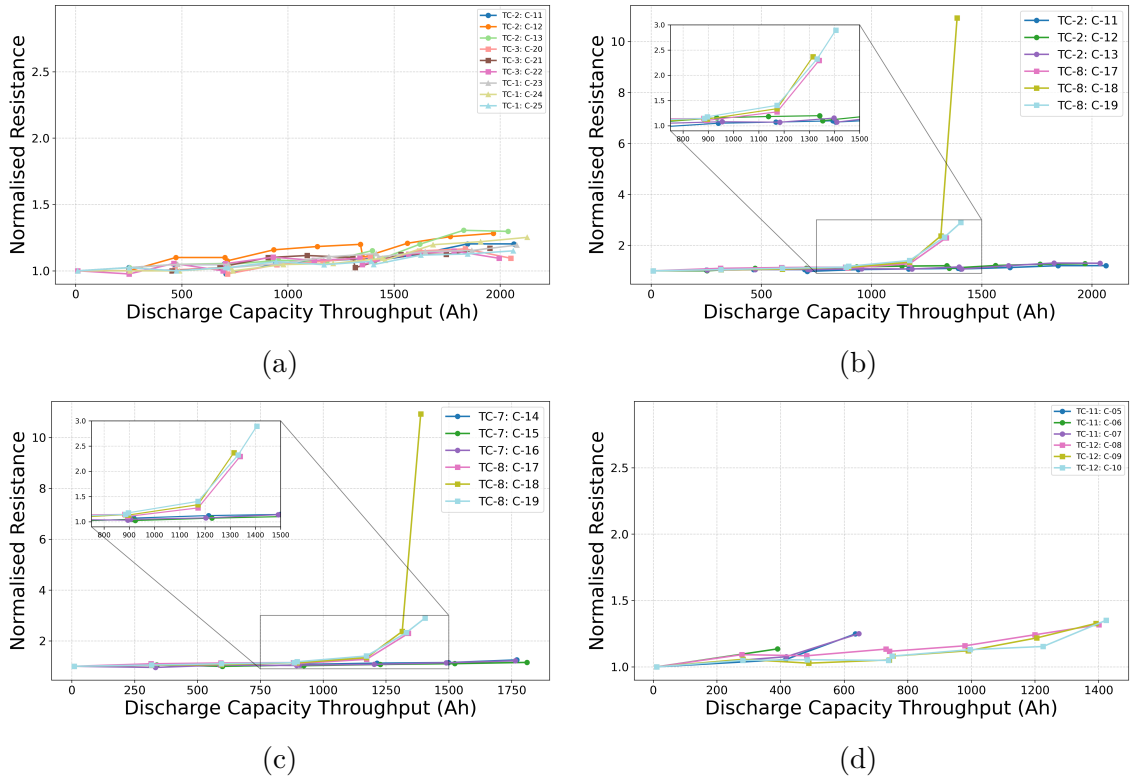

Figure 4.3: Normalised internal resistance as a function of discharge capacity throughput for different test conditions: (a) 1, 2, and 3; (b) 2 and 8; (c) 7 and 8; and (d) 11 and 12.

Table 4.2: Discharge capacity throughput and internal resistance (R_{10s}) of the cells at BOL and EOL.

Test condition	Cell ID	$Q_{TP,BOL}$ [Ah]	$Q_{TP,EOL}$ [Ah]	$R_{10s,BOL}$ [mΩ]	$R_{10s,EOL}$ [mΩ]
2	Cell 11	3.6485	3.4369	30.923	37.194
2	Cell 12	3.6764	3.3507	30.144	38.653
2	Cell 13	3.6719	3.3683	30.954	40.150
7	Cell 14	3.6525	3.2391	30.954	38.692
7	Cell 15	3.6513	3.3564	30.954	35.661
7	Cell 16	3.6438	3.2501	32.451	39.480
8	Cell 17	3.6437	1.4943	31.008	71.143
8	Cell 18	3.6453	1.2673	31.920	348.628
8	Cell 19	3.6497	1.3636	30.954	89.616
3	Cell 20	3.6597	3.4892	31.734	34.733
3	Cell 21	3.6602	3.3152	32.451	37.981
3	Cell 22	3.6624	3.4342	31.702	34.698
1	Cell 23	3.6690	3.3598	31.008	37.009
1	Cell 24	3.6592	3.4361	31.758	39.760
1	Cell 25	3.6721	3.4189	31.734	36.509

4.1.3 Incremental capacity analysis

The ICA profiles were obtained by calculating the differential capacity ($\frac{dQ}{dV}$) from the voltage and capacity data derived from the ICI measurements. To aid interpretation of the ICA profiles, peak mapping was performed by comparing the half cell profiles of the negative (Gr-SiO_x) and positive (NMC) electrodes with the corresponding full cell profile. The full cell peak positions were identified from the potential difference between the corresponding positive and negative electrode peaks. For example, the first full cell peak at 3.4 V corresponds to the difference between the first positive electrode peak at 3.65 V and the first negative electrode peak at 0.25 V. The ICA results for the fresh reference cell (Cell 03) are presented for the individual electrodes together with the corresponding BOL full cell profile of Cell 11. The negative electrode (Gr-SiO_x, inner region, PAT-1), shown in Figure 4.4a, exhibits five peaks, while the positive electrode (NMC, inner region, PAT-2), shown in Figure 4.4b, exhibits six peaks. The corresponding BOL full cell profile, presented in Figure 4.4c, contains six peaks.

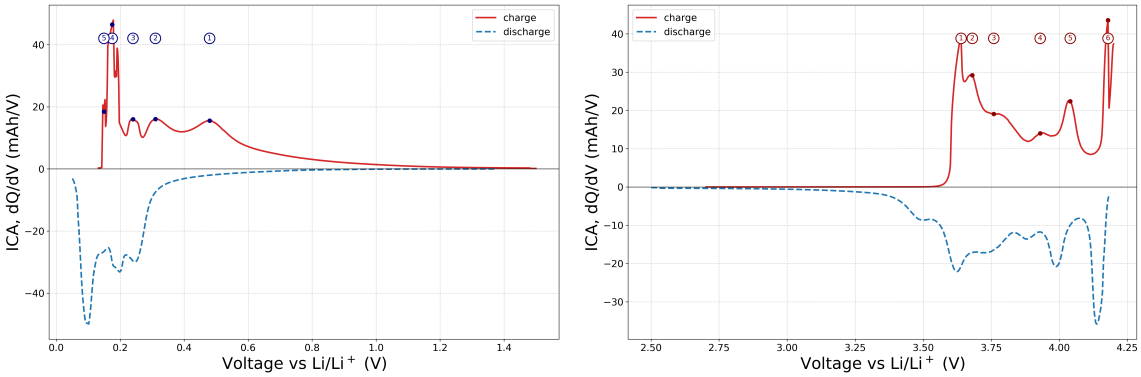

(a)

(b)

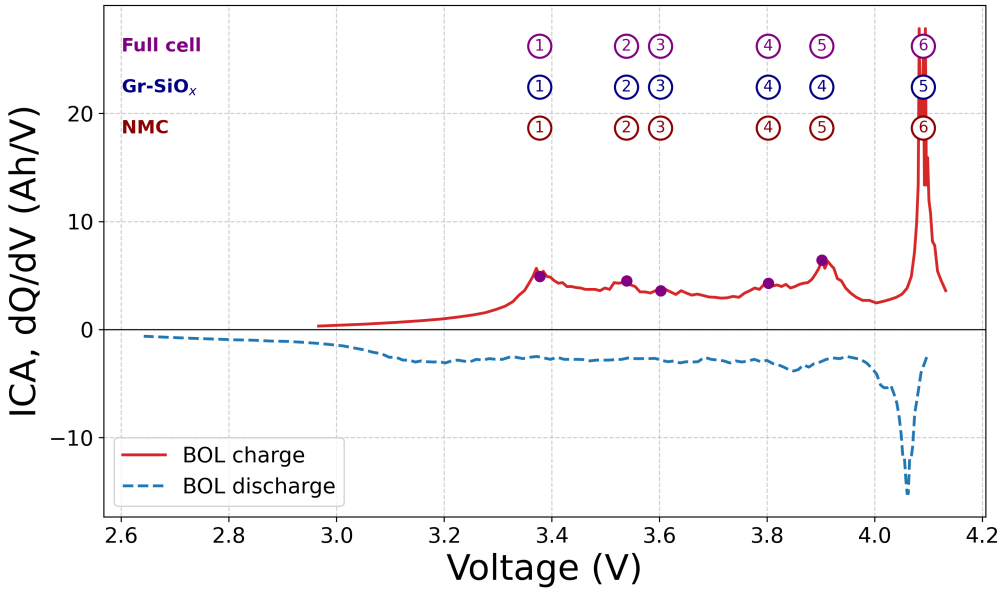

(c)

Figure 4.4: ICA of Cell 03 (PAT-1): (a) negative electrode (Gr-SiO$_x$, inner region); (b) positive electrode (NMC, outer region); and (c) BOL full cell profile of Cell 11.

For the ICA analysis, the focus was placed on the fresh reference cell (Cell 03) and two of the selected aged cells (Cells 11 and 19). The ICA profiles from BOL to EOL for Cell 11 (remaining capacity of 96%) are presented in Figure 4.5a, whereas the corresponding profiles for Cell 19 (remaining capacity of 37%) are shown in Figure 4.5b. The area under the ICA curve corresponds to the remaining capacity of the cell.

For Cell 11 (TC 2, centred voltage window), the ICA profiles largely overlap throughout the ageing process, indicating limited degradation. Only minor peak broadening, a slight reduction in the first peak at approximately 3.3 V, and a small shift in the discharge peak are observed. In contrast, Cell 19 (TC 8, lower voltage limit) exhibits progressive peak broadening, peak shifts, and reduced peak intensity with increasing ageing. The reduction in the area under the curve is also substantially greater for Cell 19. The first peak becomes significantly broader and shifts towards higher

potentials, from approximately 3.3 V for RPT1 to approximately 3.6 V for RPT8. This behaviour indicates increased polarisation, which is also consistent with the resistance increase observed in Figure 4.3b.

The ICA profiles at BOL for test conditions 2 and 8 are presented in Figure 4.5c. At BOL, all profiles overlap closely, indicating similar initial cell behaviour. In contrast, the EOL ICA profiles presented in Figure 4.5d, including the BOL reference from Cell 11 (black line), demonstrate clear differences between the two test conditions. The cells cycled under TC 2, retaining approximately 96% of their initial capacity, closely follow the BOL profile. Conversely, the cells subjected to TC 8, retaining only approximately 37% capacity, exhibit substantial peak shifts, peak broadening, and reduced peak intensity, indicating significantly more severe degradation. Although both test condition groups follow similar overall trends, the spread in TC 8 is slightly larger.

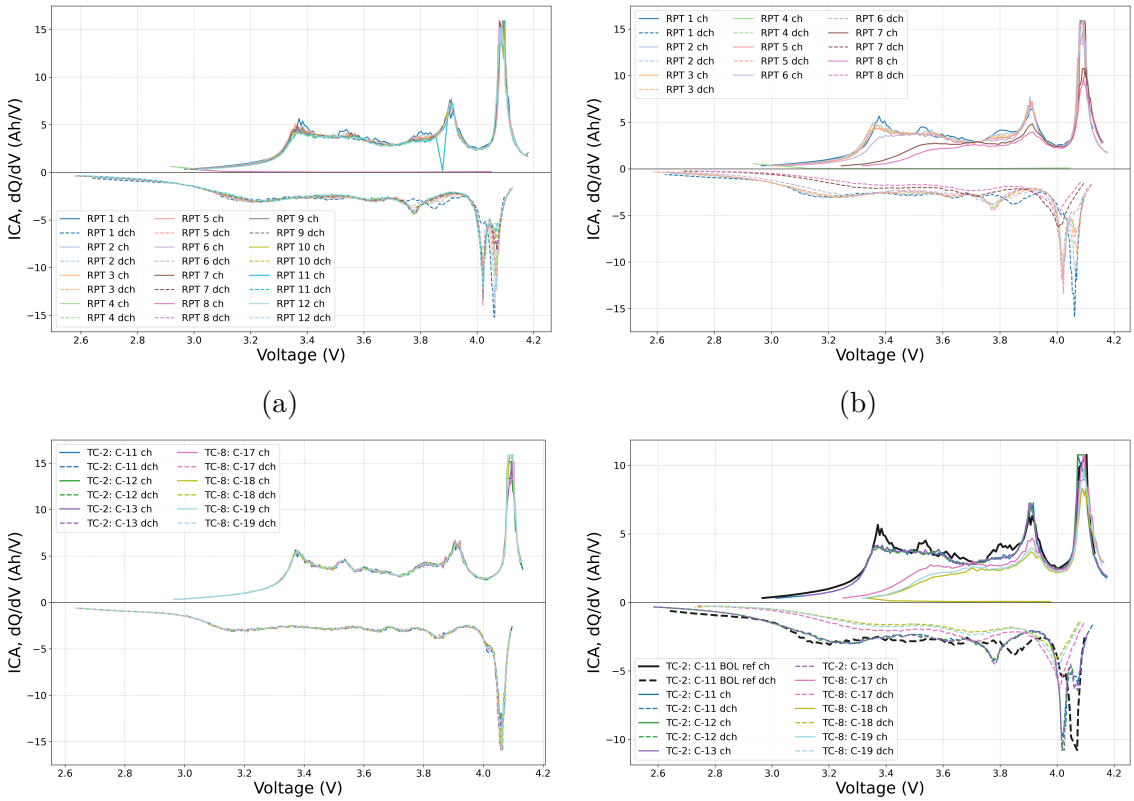

Figure 4.5: ICA (dQ/dV) as a function of voltage for: (a) test condition 2, Cell 11, all RPTs; (b) test condition 8, Cell 19, all RPTs; (c) test conditions 2 and 8 at BOL; and (d) test conditions 2 and 8 at EOL with a BOL reference from Cell 11.

4.2 Computed tomography scan

To examine the internal structure of the commercial 18650 cells, including electrode stacking, tabs, and safety features, the cells were subjected to CT scanning. In addition, the CT scans assisted the teardown process by providing information regarding the margin between the cap and the electrode overhang. Cell 19 was of particular interest due to its substantial capacity fade, as presented in Figure 4.1b.

CT scans of the BOL cell and aged Cell 19 (TC 8, lower voltage limit) are compared in Figure 4.6a, while the corresponding magnified views of the cap region are provided in Figure 4.6b. In Figure 4.6a, the negative tab of the aged cell appears bent, and slight deformation of the bottom casing can also be observed. In addition, the empty space along the central region of the jellyroll is reduced in the aged cell compared with the BOL cell. A clearer view of the cap region is presented in Figure 4.6b, where deformation of the cap structure is also visible. Furthermore, the upper thin tab within the cap appears fractured. However, part of the fractured tab remained in electrical contact with the cell, as the cell retained 37% of its capacity. Comparison with Figure 2.6 indicates that the cell remained generally well aligned, with uniformly stacked electrode layers and sufficient negative electrode overhang.

Cross-sectional CT images of BOL Cells 11 (left, TC 2, centred voltage window) and 15 (right, TC 7, higher upper voltage limit) are presented in Figure 4.7a, whereas the corresponding cross-sectional images of BOL Cell 19 (left) and aged Cell 19 (right) are shown in Figure 4.7b. As shown in Figure 4.7a, a fold is visible in the centre of the jellyroll in several fresh cells. This observation suggests a recurring manufacturing deviation. Upon ageing, the jellyroll expands, leading to a reduction in the empty space at the centre of the cell, as observed in Figure 4.7b.

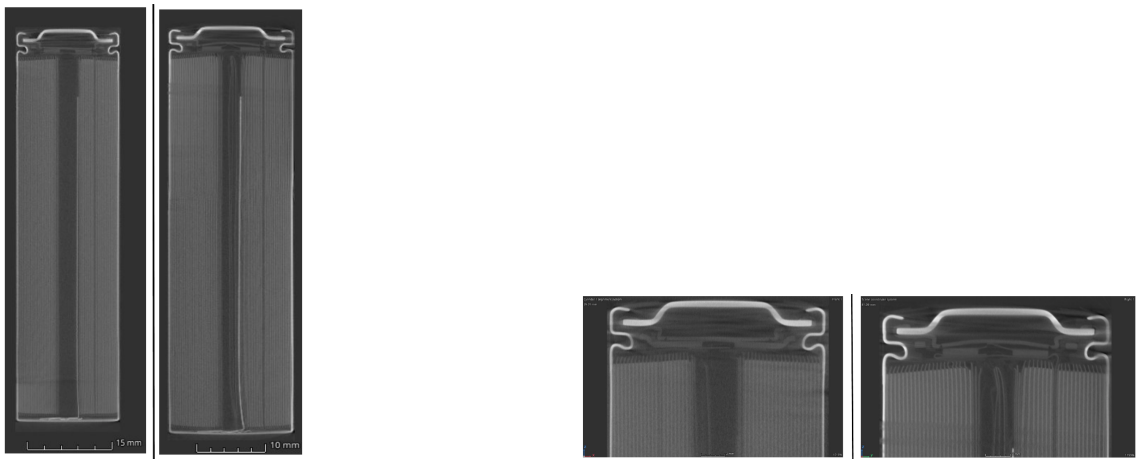

(a) (b)

Figure 4.6: CT scans comparing BOL Cell 19 (left) and aged Cell 19 (right): (a) full cell views and (b) magnified views of the cap region.

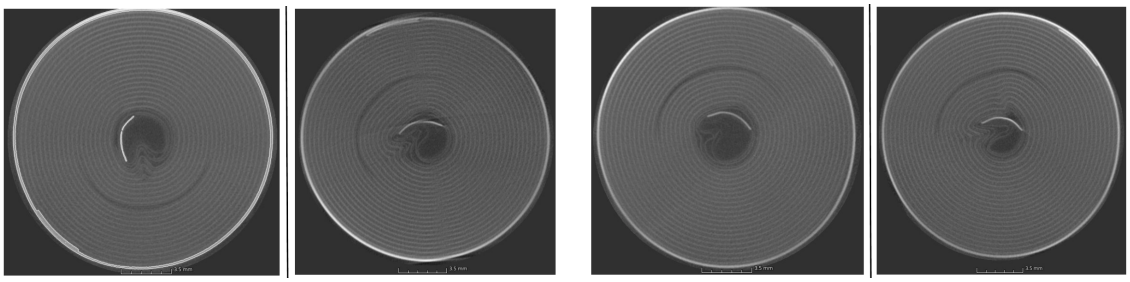

(a) (b)

Figure 4.7: CT scans of (a) cross-sections of BOL Cells 11 (left) and 15 (right); and (b) cross-sections of BOL (left) and EOL (right) Cell 19.

4.3 Design and production of tool

To enable the teardown of stainless steel cylindrical cell casings, an in-house developed tool was designed and manufactured. The fabrication of the V-cut holder and the sliding wall using a 3D printer is shown in Figure 4.8a. The fully assembled tool is presented in Figure 4.8b (side view) and Figure 4.8c (top view). The tool includes a display indicating the blade position, enabling calibration of the cutting depth into the cell casing.

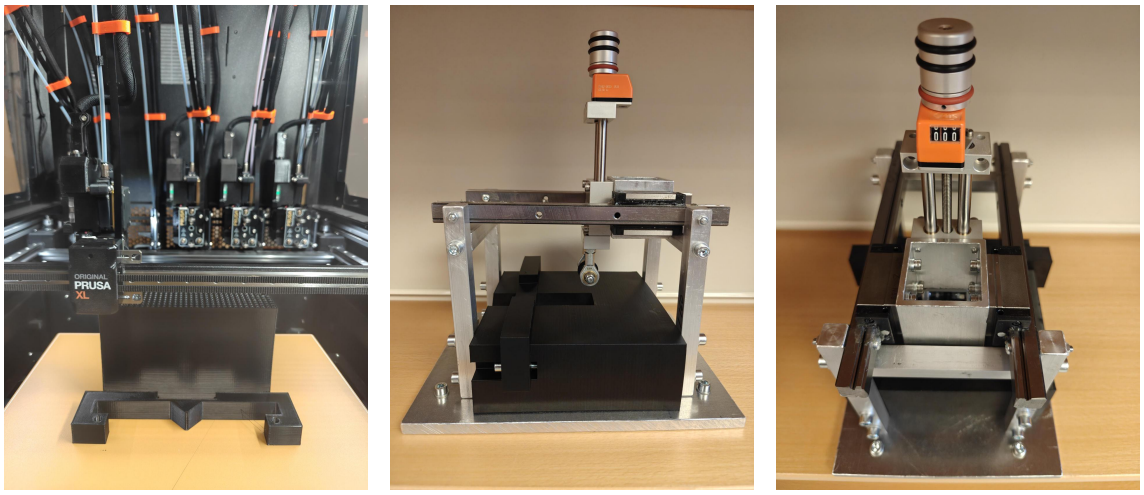

(a) (b) (c)

Figure 4.8: (a) Fabrication of a tool component using a 3D printer; (b) side view of the fully assembled in-house developed tool; and (c) positioning table in its initial position, with the display visible.

4.4 Cell teardown

Post-mortem analysis of the selected aged cells from the lifetime testing was performed in comparison with the fresh reference cell, Cell 03, whose negative electrode is presented in Figure 3.3e. Cell 11 from TC 2 (centred voltage window), Cell 15 from TC 7 (higher upper voltage limit), and Cell 19 from TC 8 (lower voltage limit) were selected for disassembly and internal inspection. At EOL, the corresponding remaining capacities were 96%, 92%, and 37%, respectively. The concave and convex sides of the negative electrode for Cell 15 are presented in Figure 4.9a and Figure 4.9b, respectively, while the corresponding surfaces for Cell 19 are shown in Figure 4.9c and Figure 4.9d. The concave side corresponds to the inner part of the cell facing towards the centre of the jellyroll, whereas the convex side corresponds to the outer part facing the cell casing. No observable differences were identified between Cell 11 and the fresh reference cell. Therefore, no images of Cell 11 are presented. Li-plating is observed across the central region of the negative electrode surface for Cell 15, whereas for Cell 19, Li-plating is predominantly visible along the electrode edges. No visible differences were observed between the fresh and aged positive electrodes. Consequently, no images of the positive electrodes are presented.

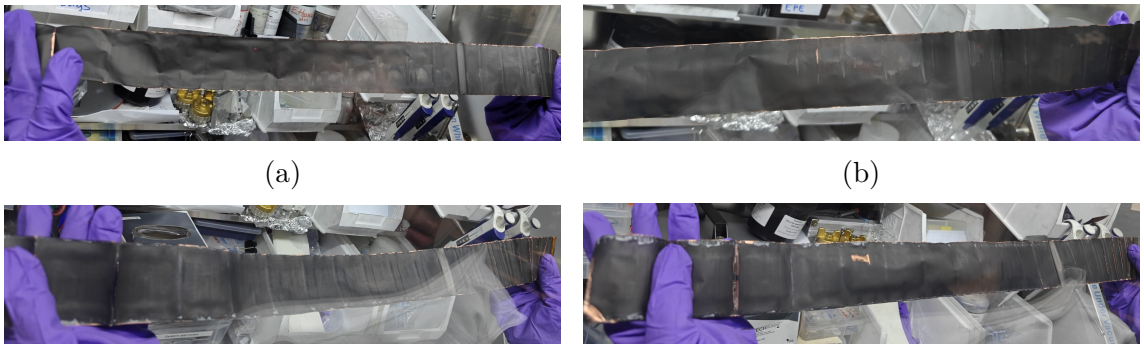

(a) (b)

(c) (d)

Figure 4.9: Concave (a, c) and convex (b, d) sides of the negative electrode for Cell 15 (a, b) and Cell 19 (c, d).

4.5 Post-mortem morphological analysis of the electrode

4.5.1 Scanning electron microscopy

Further post-mortem analysis was conducted using SEM, where micrographs of the aged cells (Cell 11, TC 2, centred voltage window; Cell 15, TC 7, higher upper voltage limit; and Cell 19, TC 8, lower voltage limit) were compared with those of the fresh reference cell (Cell 03). At EOL, the corresponding remaining capacities were 96%, 92%, and 37%, respectively. The SEM samples were obtained from the same electrode regions as the PAT-cell samples, including the inner, middle, and outer regions of the electrodes. The inner regions of the negative electrode are presented in Figure 4.10a–Figure 4.10d, while the outer regions of the positive electrode are shown in Figure 4.12a–Figure 4.12d. The middle region of the negative electrode for Cell 15 is presented in Figure 4.11. The outer regions of the negative electrode and the inner regions of the positive electrode did not exhibit significant differences among the four cells and are therefore provided in Appendix B (see Figure B.1a–Figure B.2d).

The SEM micrograph of the fresh negative electrode (Cell 03), presented in Figure 4.10a, shows graphite particles with relatively flat and well defined surfaces compared with the aged cells. In Cell 11 (remaining capacity of 96%), shown in Figure 4.10b, the graphite particles appear slightly smaller and rougher. Visible Li-plating was identified on the negative electrode of Cell 15 (remaining capacity of 92%) during the teardown process. In Figure 4.10c, several darker regions are observed, indicating either valleys in the electrode surface topography or low atomic number materials that are difficult to detect by SEM, such as Li-containing deposits. In addition, an exfoliated graphite sheet is visible, particularly in the central and right-hand regions of the micrograph, where the surface appears brighter and less homogeneous than the surrounding particles. The middle region of the negative electrode for Cell 15, presented in Figure 4.11, exhibited extensive Li-plating. Several darker regions are again visible and may correspond to lithium deposits. Furthermore, small graphite fragments are distributed across the micrograph, resulting in a mossy surface morphology. In Figure 4.10d, corresponding to Cell 19 with a remaining capacity of 37%, the graphite particles appear ruptured and porous, with dendritic surface features indicative of Li-plating covered by SEI growth.

The SEM micrograph of the fresh positive electrode (Cell 03), presented in Figure 4.12a, shows minor surface cracking of the NMC particles, although such cracking is generally more pronounced in aged cells. No major differences are observed for Cell 11 (Figure 4.12b) or Cell 15 (Figure 4.12c) compared with the fresh cell. However, the positive electrode of Cell 19, shown in Figure 4.12d, exhibits more distinct particle cracking.

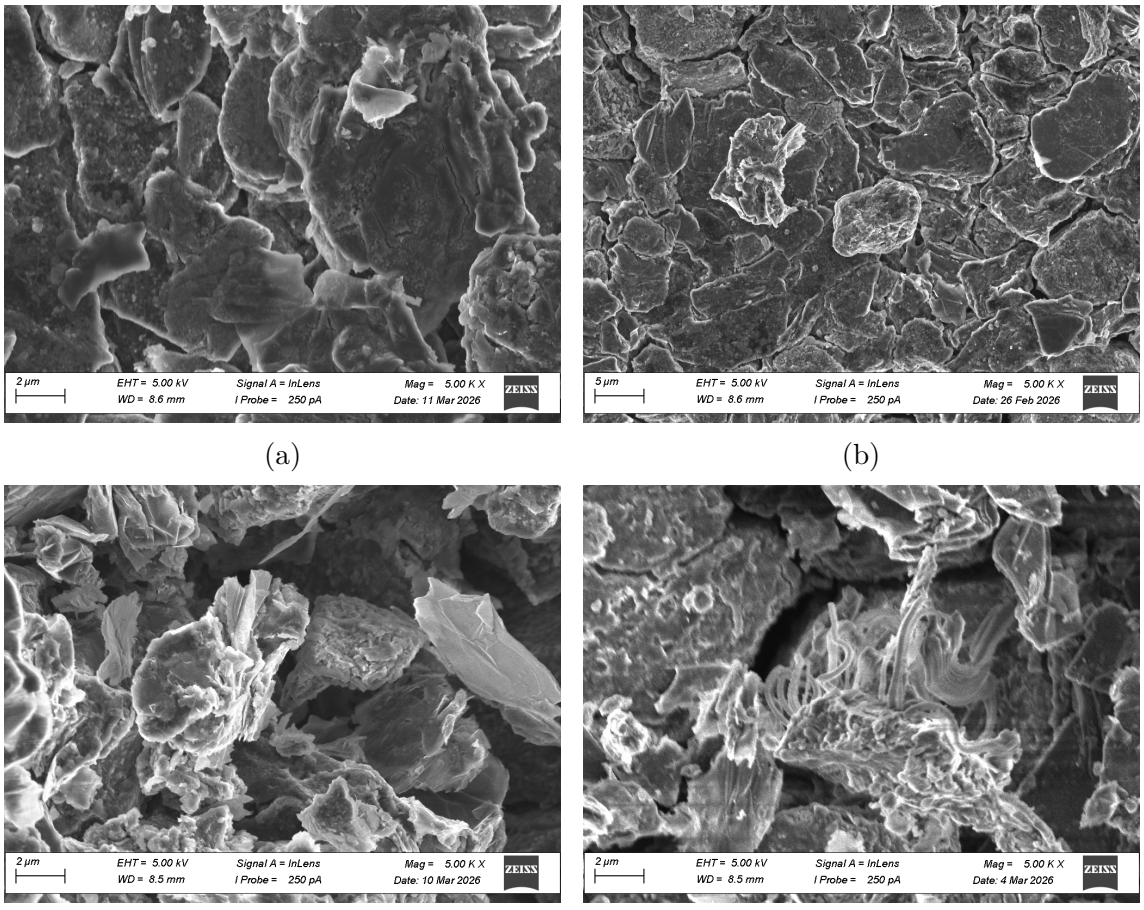

(a) (b)

(c) (d)

Figure 4.10: SEM micrographs of the inner region of the graphite negative electrode for (a) Cell 03, (b) Cell 11, (c) Cell 15, and (d) Cell 19.

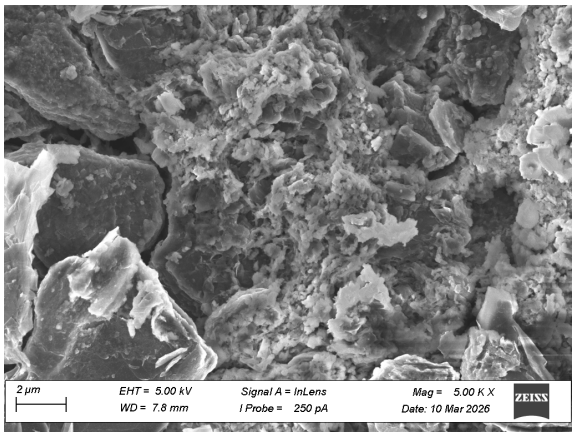

Figure 4.11: SEM micrograph of the middle region of the graphite negative electrode for Cell 15.

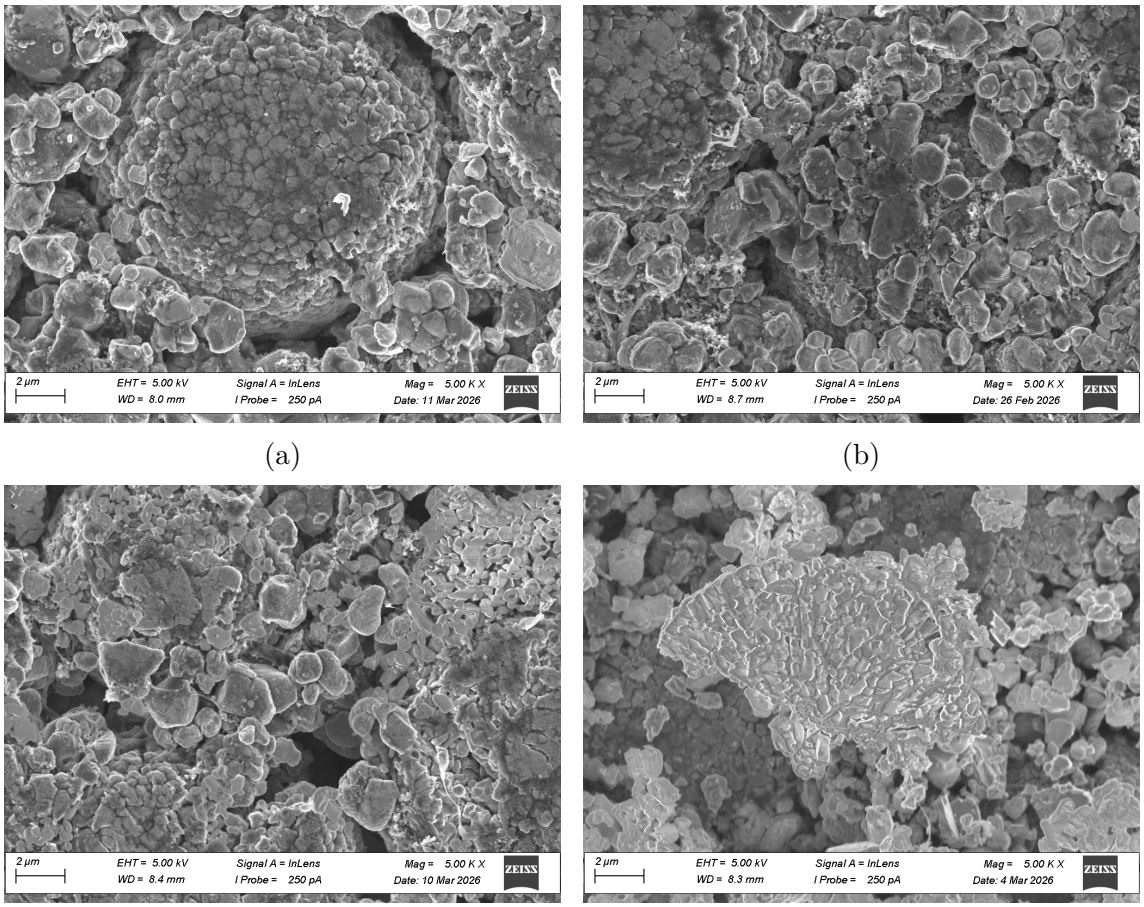

Figure 4.12: SEM micrographs of the outer region of the NMC positive electrode for (a) Cell 03, (b) Cell 11, (c) Cell 15, and (d) Cell 19.

4.5.2 Energy-dispersive X-ray spectroscopy

The EDX spectra and elemental weight percentages are not presented, since an accelerating voltage of 5 kV was used, which primarily probes the electrode surface rather than the bulk material. The EDX mapping was selected based on the regions of interest identified in the SEM micrographs and illustrates the spatial distribution of elements across the electrode surface. For the negative electrode, overlapping regions of Si and O indicate locations where SiO_x particles may be present. Five elements, C (green), O (red), Si (blue), F (yellow), and P (magenta), are shown for the negative electrode, whereas eight elements, Ni (purple), Mn (orange), Co (cyan), C (green), O (red), Al (dark blue), F (yellow), and P (magenta), are presented for the positive electrode. Accordingly, only the inner region of the negative electrode and the outer region of the positive electrode are presented. The fresh reference cell (Cell 03) is compared with Cell 15 from TC 7 (higher upper voltage limit), which exhibited visible Li-plating, and Cell 19 from TC 8 (lower voltage limit), which exhibited the most severe capacity fade. The elemental mapping of the negative electrode for Cell 03 and Cell 15 is shown in Figure 4.13a and Figure 4.13c, respectively. Similarly, the mapping of the positive electrode for Cell 03 and Cell 19 is presented in Figure 4.13b and Figure 4.13d, respectively. The corresponding mappings for Cells 11, the NMC mapping of Cell 15, and Gr-SiO_x mapping of Cell 19 are provided in the Appendix B (see Figure B.3a–Figure 4.13d).

The EDX mapping of the inner region of the negative electrode for the fresh cell (Cell 03), shown in Figure 4.13a, exhibits a relatively dense and homogeneous distribution of C, O, and Si compared with the aged cells. Carbon covers the majority of the mapped surface, while overlapping regions of O and Si correspond to the SiO_x particles. In contrast, the aged Cell 15 (remaining capacity of 92%), presented in Figure 4.13c, exhibits a less uniform carbon distribution together with larger dark regions throughout the mapping. These darker regions may correspond either to voids in the electrode structure or to Li-containing deposits that cannot readily be detected by SEM or EDX due to the low atomic number of lithium. Li-plating was observed during the teardown process, and the investigated inner region was located closer to the plated area than the outer region.

The EDX mapping of the outer region of the positive electrode for the fresh cell (Cell 03), presented in Figure 4.13b, shows a relatively dense and homogeneous distribution of Ni, Mn, Co, and O, as expected for an NMC electrode. The darker regions likely correspond to pores or voids within the porous electrode structure. For the aged Cell 19 (remaining capacity of 37%), shown in Figure 4.13d, the distributions of Ni, Mn, and Co appear less uniform compared with the fresh electrode, particularly for Mn, where a reduced signal intensity is observed.

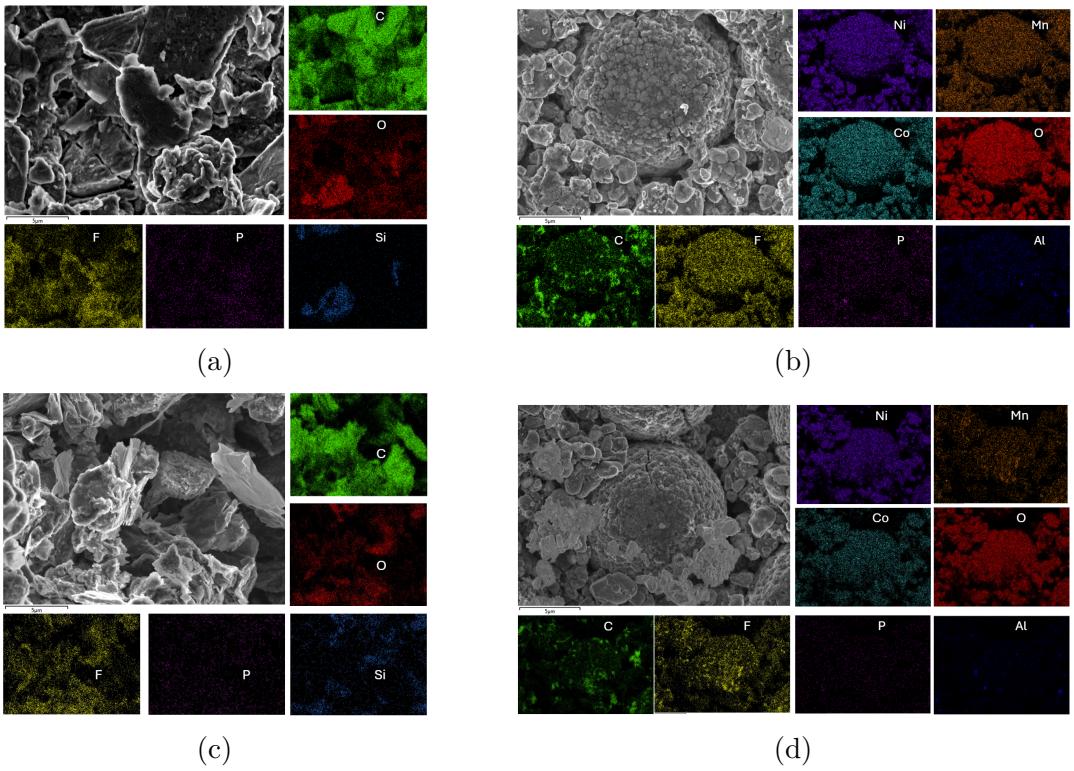

Figure 4.13: EDX mapping of the fresh reference cell (Cell 03): (a) negative electrode and (b) positive electrode. EDX mapping of the aged cells: (c) negative electrode of Cell 15 and (d) positive electrode of Cell 19.

4.6 Material characterisation of laboratory-scale cells

The electrodes harvested during the teardown process from the fresh reference cell (Cell 03) and the selected aged cells were used for the laboratory-scale PAT-cell analysis. The aged cells included Cell 11 (TC 2, centred voltage window), Cell 15 (TC 7, higher upper voltage limit), and Cell 19 (TC 8, lower voltage limit). At EOL, the corresponding remaining capacities were 96%, 92%, and 37%, respectively. The inner and outer electrode regions were investigated, corresponding to sections located 10 cm from each end of the electrode, while only the middle region of the negative electrode was examined for Cell 15. In this section, the results from PAT-1 are presented due to the higher data consistency compared with PAT-2. The capacity and impedance analyses are presented below.

4.6.1 Capacity measurement

The capacities of the aged cells (Cells 11, 15, and 19) are compared with those of the fresh reference cell (Cell 03). The inner region of the negative electrode is shown in Figure 4.14a, while the corresponding outer region of the positive electrode is presented in Figure 4.14b. Overall, Cell 11 exhibits capacity profiles closely resem-

bling those of the fresh reference cell for both the negative and positive electrodes, whereas Cells 15 and 19 show larger variations between electrode regions. An exception is observed for the inner region of the negative electrode in Cell 15, where the discharge capacity is higher than that of the fresh cell.

Cell 11 (remaining capacity of 96%) follows the fresh reference cell closely in the capacity tables for both electrodes. No major differences are observed between the inner and outer electrode regions. In contrast, Cell 15 exhibits more irregular behaviour. For the negative electrode, the outer region shows a higher capacity than the inner and middle regions, where visible Li-plating was observed during teardown. No major differences are observed between the inner and outer regions of the positive electrode for Cell 15. For Cell 19, the negative electrode exhibits a higher capacity in the inner region compared with the outer region. The positive electrode exhibits a slightly lower capacity in the inner region compared with the outer region.

Several outliers are observed in the capacity measurements. In Table 4.6, PAT-2 of Cell 03 exhibits a substantially lower capacity than PAT-1, despite both measurements originating from a fresh cell. Similarly, in Table 4.4, PAT-2 of Cell 19 exhibits a substantially lower capacity than PAT-1.

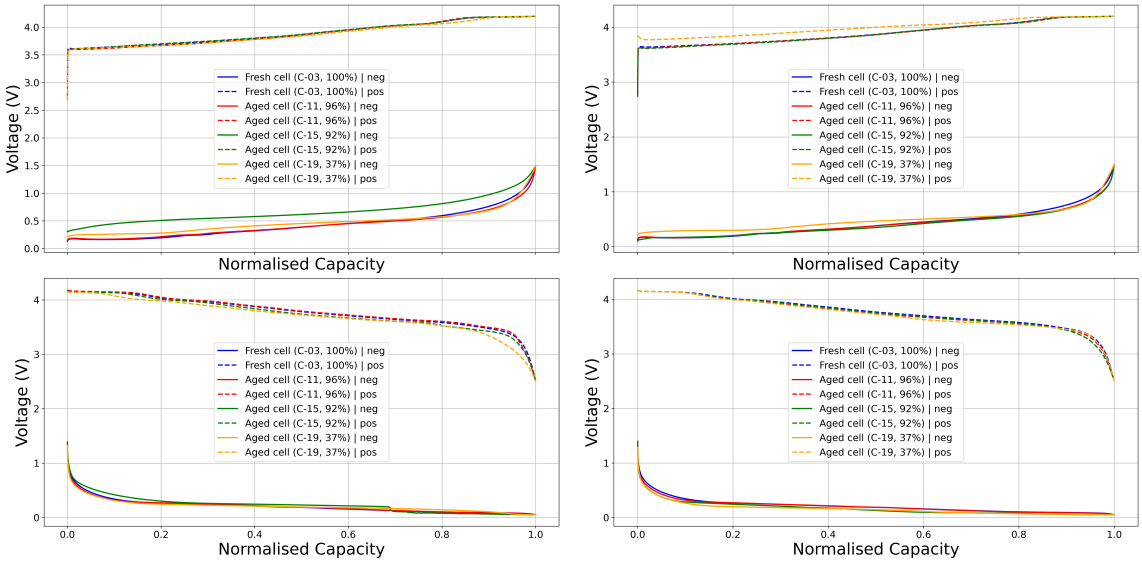

(a) (b)

Figure 4.14: Capacity profiles of Cells 03, 11, 15, and 19: (a) inner region of the negative electrode, showing charge (upper) and discharge (lower) curves; and (b) outer region of the positive electrode, showing charge (upper) and discharge (lower) curves.

The corresponding capacity values are summarised in Table 4.3 and Table 4.4 for the negative electrode in the inner (and middle) and outer regions, respectively, and in Table 4.5 and Table 4.6 for the positive electrode in the inner and outer regions. The mass values reported in the tables correspond to single coated electrodes, consisting predominantly of active material together with smaller fractions of binder and other inactive components. A double coated 18 mm disc from a fresh cell (Cell

26), together with single coated discs from Cells 03, 11, 15, and 19, were weighed for both the negative and positive electrodes. The mass contribution of the current collector was estimated by subtracting the median mass of the single coated discs from the mass of the corresponding double coated disc.

Table 4.3: Capacity measurements of the PAT-cells for fresh and aged cells in the inner and middle regions of the negative electrode.

PAT-cell (neg. inner)	Weight [mg]	Capacity [mAh]	Specific capacity [$mAhg^{-1}$]
Cell-03 PAT-1	22.7	8.040	354.185
Cell-03 PAT-2	22.3	8.011	359.238
Cell-11 PAT-1	21.0	7.749	369.000
Cell-11 PAT-2	20.6	10.134	491.942
Cell-15 PAT-1	21.3	2.983	140.047
Cell-15 PAT-2	21.4	9.482	443.084
Cell-15 middle PAT-1	26.2	8.926	340.687
Cell-15 middle PAT-2	25.3	8.655	342.095
Cell-19 PAT-1	25.0	2.899	115.96
Cell-19 PAT-2	24.9	3.174	127.470

Table 4.4: Capacity measurements of the PAT-cells for fresh and aged cells in the outer region of the negative electrode.

PAT-cell (neg. outer)	Weight [mg]	Capacity [mAh]	Specific capacity [$mAhg^{-1}$]
Cell-03 PAT-1	-	7.792	-
Cell-03 PAT-2	20.7	9.612	464.348
Cell-11 PAT-1	22.0	7.624	346.545
Cell-11 PAT-2	21.7	7.293	336.083
Cell-15 PAT-1	24.3	11.039	454.280
Cell-15 PAT-2	23.7	10.365	437.342
Cell-19 PAT-1	25.8	2.388	92.558
Cell-19 PAT-2	26.6	0.283	10.639

Table 4.5: Capacity measurements of the PAT-cells for fresh and aged cells in the inner region of the positive electrode.

PAT-cell (pos. inner)	Weight [mg]	Capacity [mAh]	Specific capacity [$mAhg^{-1}$]
Cell-03 PAT-1	62.2	11.924	191.704
Cell-03 PAT-2	61.3	11.583	188.956
Cell-11 PAT-1	63.6	11.981	188.381
Cell-11 PAT-2	65.3	11.972	183.338
Cell-15 PAT-1	62.5	11.373	181.968
Cell-15 PAT-2	62.6	11.540	184.345
Cell-19 PAT-1	61.4	10.093	164.381
Cell-19 PAT-2	63.1	10.546	167.132

Table 4.6: Capacity measurements of the PAT cells for fresh and aged cells in the outer region of the positive electrode.

PAT-cell (pos. outer)	Weight [mg]	Capacity [mAh]	Specific capacity [mAhg^{-1}]
Cell-03 PAT-1	60.9	11.182	183.612
Cell-03 PAT-2	60.5	6.977	115.322
Cell-11 PAT-1	62.3	10.950	175.762
Cell-11 PAT-2	62.6	10.214	163.163
Cell-15 PAT-1	61.2	10.571	172.729
Cell-15 PAT-2	61.6	10.822	175.682
Cell-19 PAT-1	61.1	11.238	183.928
Cell-19 PAT-2	62.0	11.556	186.387

4.6.2 Impedance analysis

Nyquist plots of the fresh reference cell (Cell 03) are compared with those of the aged cells. The aged cells included Cell 11 (TC 2, centred voltage window), Cell 15 (TC 7, higher upper voltage limit), and Cell 19 (TC 8, lower voltage limit). For the negative electrode, the inner region is presented in Figure 4.15a, with the corresponding values of ohmic resistance (R_s) and charge transfer resistance (R_{ct}) summarised in Table 4.7. The outer region is shown in Figure 4.15b, with the corresponding resistance values provided in Table 4.8. For the positive electrode, the inner region is presented in Figure 4.15c, with the corresponding R_s and R_{ct} values summarised in Table 4.9. The outer region is shown in Figure 4.15d, with the corresponding resistance values presented in Table 4.10. The results from PAT-1 are presented here due to their higher consistency, while the Nyquist plots for the PAT-2 cells are provided in the Appendix B (see Figure B.4a–Figure B.4d).

For the inner region of the negative electrode, shown in Figure 4.15a, the aged cells generally exhibit larger semicircle diameters than the fresh reference cell, corresponding to increased charge transfer resistance, R_{ct}. Cell 11 (remaining capacity of 96%) is the only exception, exhibiting a slightly smaller semicircle than the fresh Cell 03. A notable observation is that the middle region of Cell 15, corresponding to the visibly Li-plated area, exhibits a smaller semicircle than the inner region of the same cell, despite the latter showing less obvious Li-plating. The inner region exhibits an approximately 10 Ω larger semicircle diameter than the middle region. Another unexpected result is that Cell 15 exhibits an approximately 5 Ω larger semicircle than Cell 19, despite Cell 19 experiencing substantially greater capacity fade. In contrast, the outer region of the negative electrode, presented in Figure 4.15b, follows the expected ageing trend more closely, where the cell with the lowest remaining capacity exhibits the largest semicircle. The inset additionally shows that Cells 11 and 15 exhibit semicircle shapes similar to that of the fresh cell. For both the inner and outer regions of the negative electrode, the ohmic resistance, R_s, begins at approximately the same position for all cells.

The inner region of the positive electrode is presented in Figure 4.15c. In this case, the R_s values begin at different positions. The fresh cell together with Cells 11 and 15 start at similar positions, as highlighted in the inset, whereas Cell 19 exhibits an approximately 6 Ω shift. The R_{ct} values are similar for the fresh cell and Cell 11, whereas Cell 15 exhibits an approximately 4 Ω increase in semicircle diameter and Cell 19 an increase of approximately 23 Ω. The outer region of the positive electrode, shown in Figure 4.15d, exhibits slightly larger semicircles for Cells 11 and 15 compared with the fresh cell. In this region, Cell 19 does not follow the expected ageing trend, as the increase in R_{ct} is smaller than anticipated based on the degree of capacity fade. However, the R_s values begin at approximately the same position for all cells.

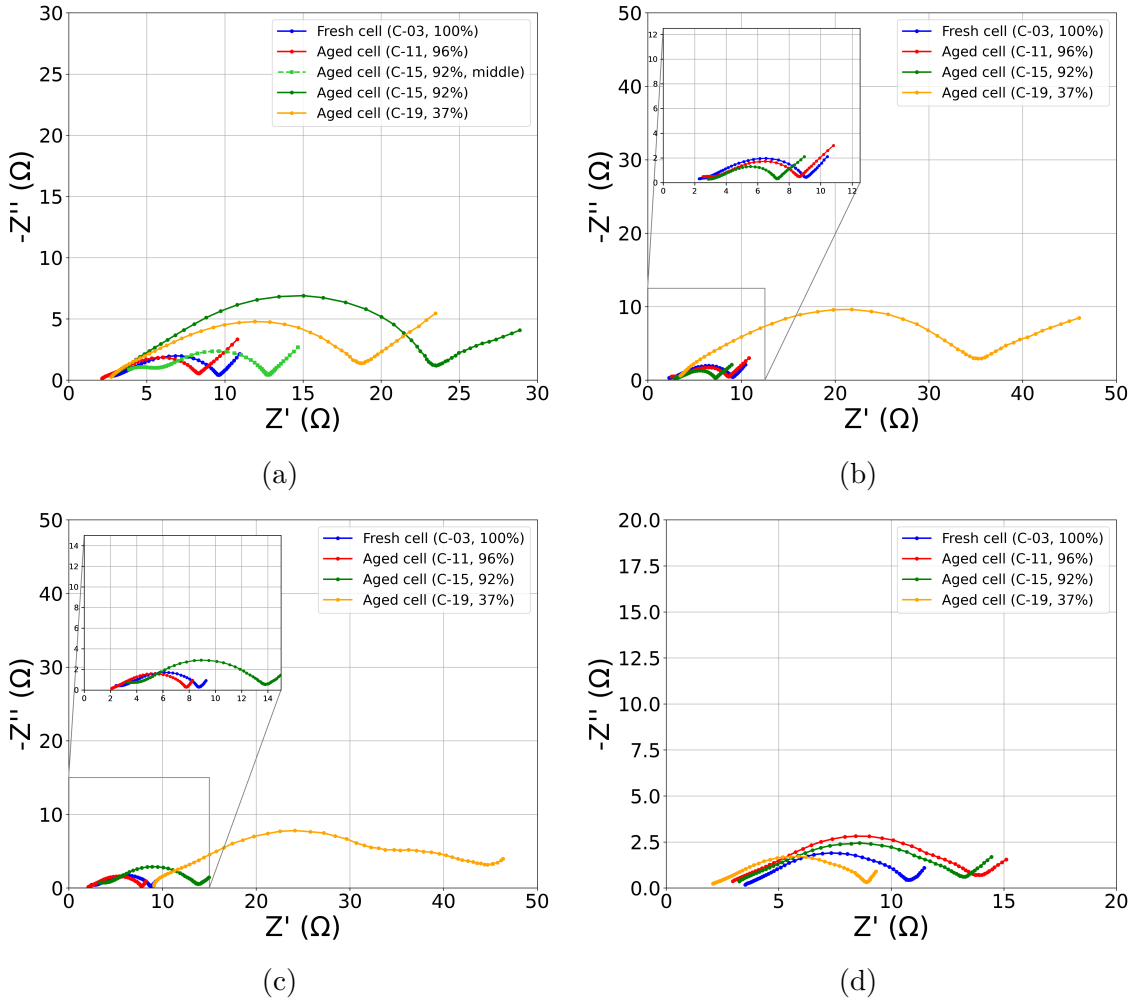

Figure 4.15: EIS of Cells 03, 11, 15, and 19: (a) inner and (b) outer regions of the negative electrode; and (c) inner and (d) outer regions of the positive electrode.

Table 4.7: Internal resistance measurements of the PAT-cells for fresh and aged cells in the inner and middle regions of the negative electrode.

PAT-cell (neg. inner)	R_s [Ω]	R_{ct} [Ω]
Cell-03 PAT-1	2.6967	6.8584
Cell-03 PAT-2	2.3084	7.1916
Cell-11 PAT-1	2.1269	6.2065
Cell-11 PAT-2	2.3068	6.3699
Cell-15 PAT-1	3.0090	20.4460
Cell-15 PAT-2	3.0894	4.8532
Cell-15 middle PAT-1	3.8688	9.1312
Cell-15 middle PAT-2	3.4082	8.6630
Cell-19 PAT-1	2.7114	16.0319
Cell-19 PAT-2	6.5551	15.4278

Table 4.8: Internal resistance measurements of the PAT-cells for fresh and aged cells in the outer region of the negative electrode.

PAT-cell (neg. outer)	R_s [Ω]	R_{ct} [Ω]
Cell-03 PAT-1	2.2940	6.7772
Cell-03 PAT-2	2.5311	7.1599
Cell-11 PAT-1	2.5328	6.4672
Cell-11 PAT-2	2.7348	6.2652
Cell-15 PAT-1	2.8548	4.3806
Cell-15 PAT-2	2.2824	4.7176
Cell-19 PAT-1	3.4863	31.7881
Cell-19 PAT-2	21.7147	118.9773

Table 4.9: Internal resistance measurements of the PAT-cells for fresh and aged cells in the inner region of the positive electrode.

PAT-cell (pos. inner)	R_s [Ω]	R_{ct} [Ω]
Cell-03 PAT-1	2.4227	6.3296
Cell-03 PAT-2	2.4072	7.5016
Cell-11 PAT-1	2.0893	5.6787
Cell-11 PAT-2	6.1040	5.8960
Cell-15 PAT-1	3.2773	10.2227
Cell-15 PAT-2	3.0897	6.2852
Cell-19 PAT-1	9.0914	35.6096
Cell-19 PAT-2	6.1788	12.9837

Table 4.10: Internal resistance measurements of the PAT-cells for fresh and aged cells in the outer region of the positive electrode.

PAT-cell (pos. outer)	R_s [Ω]	R_{ct} [Ω]
Cell-03 PAT-1	3.5115	7.2641
Cell-03 PAT-2	1.6164	8.8835
Cell-11 PAT-1	2.9552	10.9595
Cell-11 PAT-2	4.0177	10.9823
Cell-15 PAT-1	3.2444	10.0312
Cell-15 PAT-2	3.6103	6.8897
Cell-19 PAT-1	2.0800	6.8419
Cell-19 PAT-2	5.4245	6.5755

4.6.3 Incremental capacity analysis

The ICA profiles were obtained from the inner region PAT-1 for the negative electrode and from the inner region PAT-2 for the positive electrode. The ICA profiles of the aged cells, Cells 11, 15, and 19, are compared with those of the fresh reference cell, Cell 03. For the negative electrode (Figure 4.16a), the aged cells generally follow the expected ageing trend. Cell 11 from TC 2 (centred voltage window) overlaps closely with the fresh reference cell, indicating limited degradation. In contrast, Cell 15 from TC 7 (higher upper voltage limit) exhibits more pronounced peak shifts, peak broadening, and reduced peak intensity. Cell 19 from TC 8 (lower voltage limit), which exhibited the greatest capacity fade, follows a similar overall trend to Cell 15, although the changes are less pronounced. Meanwhile, the ICA profiles of the positive electrode follow trends more similar to those of the fresh reference cell, as shown in Figure 4.16b.

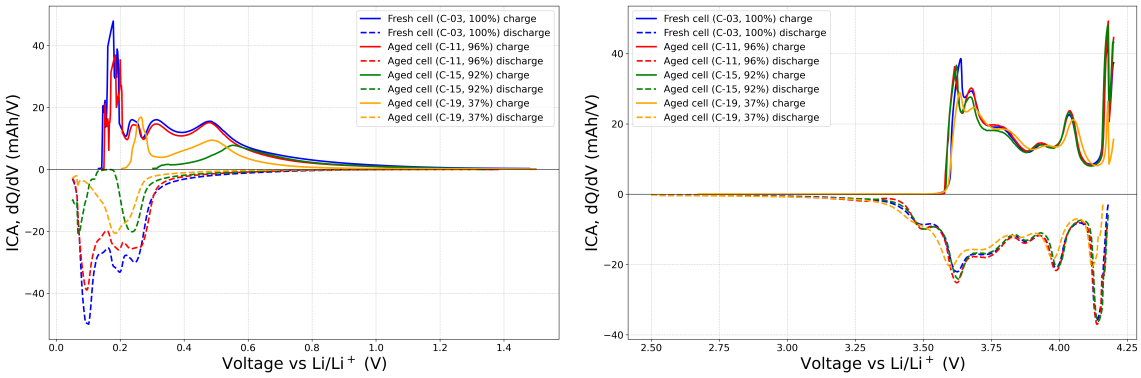

(a) (b)

Figure 4.16: ICA profiles of the inner electrode regions for (a) the negative electrode PAT-1 and (b) the positive electrode PAT-2.

5
Discussion

Detailed information regarding the various test conditions is provided in Table 3.3. TCs 1, 2, and 3 were compared to examine the influence of charge C-rate while maintaining the same voltage window width and placement. The comparison between TCs 2 and 8 was conducted to evaluate the influence of voltage window width. Similarly, the comparison between TCs 7 and 8 was intended to investigate the effect of voltage window placement, as both conditions employed the same voltage window width. The analyses primarily focus on the selected cells, including the fresh reference cell (Cell 03) and the aged cells (Cell 11 from TC 2, Cell 15 from TC 7, and Cell 19 from TC 8). TC 2 employed a 60% SOC window positioned around the middle of the full voltage range. In contrast, TCs 7 and 8 both employed an 80% SOC window, where TC 7 used the upper voltage limit and TC 8 used the lower voltage limit of the full voltage range. All three TCs were cycled using a charge C-rate of 0.8C.

5.1 Beginning of life behaviour

The cells exhibited similar behaviour in both impedance measurements (Figure 4.2a) and ICA profiles at BOL (Figure 4.5c). In addition, the cells within each test condition followed similar trends in both capacity fade and resistance growth, as shown in Figure 4.1a and Figure 4.3b, respectively. This indicates consistent manufacturing quality and uniform electrochemical behaviour at BOL. Furthermore, the CT scans (Figure 4.6b) show well aligned and uniformly stacked electrode layers. However, the folding observed in the fresh cells (Figure 4.7a) likely represents a manufacturing defect, as such deformation may increase the mechanical stress on the electrodes during ageing. This is particularly important for SiO_x-containing negative electrodes, where the Si can undergo volumetric changes of up to approximately 300% during lithiation and delithiation. Therefore, the BOL reference cells were considered reliable for comparison throughout this work.

5.2 Lifetime testing

The capacity fade observed for TCs 1, 2, and 3 (Figure 4.1c) does not exhibit a clear dependence on test condition, as all cells retained more than 90% of their initial capacity and the capacity retention curves closely overlap. These test conditions employed the same voltage window placement, centred within the full voltage range, and a 60% SOC window, while differing only in charge C-rate. This indicates that, within the investigated range of charge C-rates, the charge C-rate had a comparatively minor influence on ageing behaviour. The observed degradation is likely dominated by gradual SEI growth and continued SEI reformation during cycling. Repeated rupture and reformation of the SEI layer consume cyclable lithium and contribute to both capacity fade and increased internal resistance. As shown in the full cell impedance analysis (Figure 4.2b), the charge transfer resistance, R_{ct}, increased substantially more than the ohmic resistance, R_s, indicating that the interfacial charge transfer kinetics were more sensitive to ageing than purely ohmic transport processes. Similarly, the resistance growth trends for TCs 1, 2, and 3 (Figure 4.3a) show only minor differences between the test conditions, with all cells remaining below approximately 1.5 times their initial resistance. Such behaviour has previously been reported for mild cycling conditions, where an initial reduction in impedance may occur prior to a gradual increase later in the lifetime [46]. These results suggest that cells cycled within voltage windows centred around the middle of the allowable voltage range exhibited the slowest ageing behaviour.

The mild ageing behaviour observed for TCs 1–3 is further supported by the post-mortem analysis of Cell 11 from TC 2, including full cell impedance measurements, ICA profiles, cell teardown, SEM, EDX, and PAT-cell characterisation. During the teardown process, no clearly visible ageing features were observed on the electrodes of Cell 11. Similarly, the ICA profiles throughout the RPTs (Figure 4.5a) closely followed the BOL reference, with only minor peak shifts in the discharge profile and slight reductions in peak intensity at EOL. The SEM micrographs of the inner region of the negative electrode (Figure 4.10b) showed only slightly smaller graphite particles compared with the fresh reference cell (Cell 03), while the positive electrode (Figure 4.12b) exhibited no significant differences. In addition, the EDX mapping of the negative electrode (Figure B.3a) showed that the investigated surface remained predominantly covered by carbon, indicating that the graphite structure was largely preserved. Only a limited amount of SiO_x was detected on the analysed surface. Furthermore, the capacities measured for both the positive and negative electrode PAT cells remained close to those of the fresh reference cell (Table 4.3–Table 4.6), further confirming that most of the initial capacity was retained after cycling.

The impedance measurements of the PAT cells further support the relatively mild ageing behaviour of Cell 11. For both the negative and positive electrodes (Figure 4.15a–Figure 4.15d), the high frequency intercept corresponding to the ohmic resistance, R_s, remained similar to that of the fresh reference cell. However, slight increases in the semicircle diameter were observed, indicating a moderate increase in charge transfer resistance, R_{ct}. In this case, the flattened semicircle is likely as-

sociated with SEI growth. Most of the investigated regions followed the expected ageing trend, where increased degradation corresponded to larger semicircle diameters. However, the outer region of the positive electrode (Figure 4.15d) did not fully follow this behaviour. This may indicate that the analysed region did not represent the most severely degraded part of the electrode, although the possibility of local PAT-cell variability cannot be excluded. Such behaviour is plausible in post-mortem PAT-cell impedance measurements, since only selected regions of the jellyroll are analysed. Overall, the local variations observed between electrode regions and duplicate PAT-cells indicate that the ageing process was not entirely uniform across the jellyroll. These observations further support that cells cycled within a centred voltage window experienced comparatively mild and more homogeneous ageing than cells subjected to more aggressive voltage window placements.

In contrast to TCs 1–3, the capacity fade exhibited a clear dependence on voltage window placement for the comparisons between TCs 2 and 8, and between TCs 7 and 8, as shown in Figure 4.1a and Figure 4.1b, respectively. TC 8 deviated substantially from the other test conditions, retaining only approximately 37% of its initial capacity, whereas the remaining cells retained more than 90%. All test conditions are expected to undergo gradual SEI formation during cycling. However, the more aggressive voltage window placements in TCs 7 and 8 likely accelerated the degradation processes. The higher upper voltage limit used in TC 7 may promote electrolyte oxidation and increased interfacial degradation at high SOC. As the cell voltage increases, the negative electrode approaches potentials closer to 0 V vs. Li/Li^+, increasing the likelihood of Li-plating.

TC 8 operated closer to the lower voltage limit, resulting in higher lithiation and delithiation of the SiO_x-containing negative electrode. Such cycling conditions likely increase the volumetric strain of the active material, promoting particle cracking, SEI rupture and reformation, loss of cyclable lithium, and increased impedance. These effects are particularly severe in Si-containing negative electrodes due to the large volumetric changes associated with lithiation and delithiation. Furthermore, TC 8 exhibited a relatively abrupt capacity drop, where the state of health (SOH) decreased rapidly from approximately 90% to 40%. This behaviour may indicate that the cell reached a local mechanical or electrochemical instability rather than undergoing purely gradual ageing. Repeated volume expansion and contraction of the SiO_x-containing negative electrode may have promoted particle cracking, loss of electrical contact, accelerated SEI growth, and rapid loss of cyclable lithium once a critical degradation threshold was reached. The fold observed in the centre of the jellyroll may also have contributed to increased local mechanical stress and heterogeneous degradation. Despite the wider voltage window employed in TC 7, the capacity fade and resistance growth remained relatively similar to those of TC 2. TC 8, however, exhibited substantially more severe degradation, despite operating within the same voltage window width as TC 7. These observations indicate that voltage window placement had a greater influence on ageing behaviour than the voltage window width itself under the investigated conditions.

The severe local degradation associated with TC 7 is further supported by the post-mortem analysis of Cell 15, where Li-plating was clearly visible in the central region of the negative electrode (Figure 4.9b). This may also explain the depressed semicircle observed in the full cell impedance measurements (Figure 4.2b), likely caused by non-uniform SEI thickness and local variations in lithium concentration across the electrode surface. In addition, the increased capacity measured for the inner region negative electrode PAT-cell may be associated with partially reversible Li-plating contributing additional cyclable lithium during discharge. Furthermore, the graphite sheet previously identified in the SEM micrographs (Figure 4.10c) is also clearly visible in the EDX mapping (Figure 4.13c), particularly in the central and right-hand regions, where dense carbon rich areas are observed. In contrast, the Si signal is substantially reduced, accompanied by a noticeable decrease in oxygen content compared with the fresh reference cell. This behaviour is consistent with degradation and consumption of the SiO_x material during cycling. The presence of F and P is likely associated with decomposition products originating from the $LiPF_6$ based electrolyte and subsequent SEI formation. Compared with the fresh reference cell, Cell 15 exhibits a more heterogeneous and patchy elemental distribution, indicating localised degradation across the electrode surface.

However, the lower voltage limit employed in TC 8 appears to impose substantially more severe degradation on the negative electrode. Consequently, the degradation associated with deep lithiation outweighs the effects caused by the moderate increase in upper voltage limit observed for TC 7. Such behaviour is typical for graphite based Li-ion cells. Previous studies have similarly shown that Gr-SiO_x electrodes age more rapidly when cycled at lower voltages, mainly due to the large volumetric expansion and contraction of the SiO_x during lithiation and delithiation. These repeated volume changes accelerate SEI rupture and reformation, mechanical degradation, and loss of cyclable lithium [34].

The severe degradation of Cell 19 is further supported by the ICA profiles (Figure 4.5b and Figure 4.5d). The significant reduction of the first peak on the left side of the charge profile is associated with SEI growth, while the overall decrease in peak intensity indicates loss of cyclable lithium and active material. In addition, the shift of the first discharge peak towards higher polarisation suggests increased impedance, consistent with the resistance growth observed in the impedance analysis. Peak broadening further indicates increased heterogeneity, non-uniform lithiation, and diffusion limitations. Unlike Cell 15, where Li-plating was concentrated near the centre of the electrode, Cell 19 exhibited Li-plating predominantly along the electrode edges (Figure 4.9d). Furthermore, the lower capacities measured for the inner region of PAT cells compared with the outer region suggest more severe interfacial degradation within the inner region, despite the less pronounced visible Li-plating. Such degradation likely includes thicker SEI layers, dead lithium formation, electrolyte decomposition products, loss of electrical contact, and mechanical degradation. This suggests that the plated regions experienced substantial irreversible degradation and loss of lithium inventory, rather than predominantly reversible Li-plating.

The PAT-cell ICA profiles of the negative electrode further support the heterogeneous ageing behaviour identified in the full cell measurements (Figure 4.16a). Cell 11 (TC 2) exhibited profiles closely overlapping with the fresh reference cell, indicating limited degradation. In contrast, Cell 15 (TC 7) showed more pronounced peak shifts, peak broadening, and reduced peak intensity than Cell 19 (TC 8), despite Cell 19 exhibiting substantially greater full cell capacity fade. This behaviour suggests that localised degradation associated with Li-plating and interfacial instability was more pronounced in the analysed region of Cell 15. Meanwhile, the ICA profiles of the positive electrode remained comparatively similar to those of the fresh reference cell (Figure 4.16b), further indicating that the dominant degradation processes primarily occurred on the negative electrode.

The heterogeneous ageing behaviour of Cell 19 is further supported by the significant capacity difference between PAT-1 and PAT-2 in the inner region (Table 4.3). This observation is consistent with both the SEM micrographs and the EDX elemental mapping, which revealed non-uniform degradation across the electrode surface. In contrast to Cells 11 and 15, Cell 19 also exhibited visible degradation features on the positive electrode (Figure 4.12d), consistent with its severe capacity fade. Although the dominant degradation processes were associated with the negative electrode, Cell 19 also exhibited signs of positive electrode degradation. The particle cracking observed in the SEM micrographs may contribute to local loss of active material and electrical contact. In addition, the EDX mapping revealed a reduced Mn signal intensity compared with the fresh electrode, suggesting possible local compositional changes within the NMC electrode associated with ageing. Mn dissolution is commonly associated with ageing in NMC electrodes and may also contribute to the observed degradation behaviour [47].

Li-plating on the negative electrode was visually more pronounced in Cell 15 than in Cell 19, despite the substantially larger capacity fade observed for Cell 19. This indicates that the visible extent of Li-plating alone does not directly determine the degree of capacity loss. In Cell 15, part of the plated lithium may have remained electrochemically reversible or still visible at the time of teardown. In contrast, the more severe capacity fade observed for Cell 19 likely originated from more extensive irreversible degradation and lithium inventory loss. In addition, the concave side of the electrode, corresponding to the side facing the centre of the jellyroll during winding, exhibited more pronounced Li-plating than the convex side facing the casing. This behaviour is shown in Figure 4.9a and Figure 4.9b for Cell 15, and in Figure 4.9c and Figure 4.9d for Cell 19. These observations further support that the ageing was not uniformly distributed across the electrode. The mossy and dendritic surface morphologies observed in the SEM micrographs are commonly associated with non-uniform lithium deposition during cycling and may contribute to increased impedance, loss of cyclable lithium, and accelerated degradation.

During unfolding of the jellyroll, partial delamination and exfoliation of the electrode coating were observed, indicating mechanical degradation caused by repeated lithiation and delithiation. In contrast, the positive electrode appeared largely unchanged relative to the fresh reference cell, with no clearly visible signs of ageing. This suggests that the negative electrode experienced substantially greater mechanical stress, most likely associated with the large volumetric changes of the SiO_x particles during cycling, which may reach up to approximately 300%.

5.3 Experimental considerations and limitations

One of the main challenges during the cell teardown process was opening the stainless steel casing before the in-house tool had been developed. In addition, the thin electrode foils were highly delicate, which complicated the electrode extraction process during PAT-cell preparation. Care was required during the sandpaper treatment to avoid damaging the metal current collectors. Furthermore, the selected electrode regions were limited to approximately 50 mm in width and 65 mm in length in order to produce single coated PAT-cell discs with a diameter of 18 mm. Consequently, only two replicas could be prepared from each investigated region, since complete removal of the electrode coating across the entire electrode area was difficult to achieve.

Additional challenges were encountered during the SEM and EDX analyses. Conductive samples were required for stable SEM imaging, since non-conductive samples would otherwise require gold sputtering to suppress charging effects. The first sample investigated was double coated, which resulted in substantial charging during SEM imaging. Therefore, the remaining SEM samples were instead prepared from electrodes where one side of the coating had already been removed during PAT-cell preparation. This significantly improved the image stability and eliminated the charging effect. Furthermore, the Aztec software used for the EDX analysis did not function properly for the positive electrode data and was unable to correctly display Ni, Mn, and Co in the EDX spectra. In contrast, all expected elements were successfully detected for the negative electrode. In addition, at an accelerating voltage of 5 keV, EDX primarily probes the near surface region of the material and therefore cannot accurately determine the bulk elemental composition throughout the electrode thickness. For depth sensitive structural analysis, X-ray diffraction (XRD) would be more suitable. Consequently, the EDX mapping provided more informative results in the present study.

5.4 Design and production of the tool

A dedicated tool for opening stainless steel casings was important, as manual disassembly relying solely on physical force is neither practical nor reproducible. The in-house developed tool was straightforward to operate and significantly reduced the teardown time from approximately 1–2 h to 15–30 min. The longitudinal cutting step performed using the developed tool required only about 5 min, whereas the conventional peeling process represented the most time consuming stage of the

teardown procedure, typically requiring 1–2 h. Consequently, the developed tool substantially improved the efficiency and reproducibility of the teardown process.

However, one limitation of the tool was that the longitudinal cut penetrated the outer three layers of the jellyroll. The positioning table was initially set to 13.0 mm, which only cut through the external plastic layer of the casing, after which the cutter depth was increased to 13.5 mm. Since the casing thickness was approximately 0.2 mm, a cutting depth of 13.2 mm was insufficient to fully penetrate the stainless steel casing. In the present study, this limitation did not significantly affect the experimental work, as two PAT-cell discs with a diameter of 18 mm could still be produced from the remaining electrode width of approximately 50 mm. In contrast, the conventional peeling technique does not damage the electrode layers during disassembly.

5.5 Conclusion

This thesis investigated the cycling performance and ageing behaviour of commercial 18650 Li-ion cells with a SiO_x-containing negative electrode under different voltage window placements, voltage window widths, and charge C-rates. The results demonstrated that voltage window placement had a substantially greater influence on ageing than either voltage window width or charge C-rate under the investigated conditions. Cells cycled within a centred voltage window (TC 2) exhibited relatively mild degradation, whereas cells cycled closer to the upper or lower voltage limits (TC 7 and TC 8) showed significantly more severe ageing behaviour. The degradation was primarily associated with the negative electrode. Cycling at a higher upper voltage limit (TC 7) promoted Li-plating, while cycling at a lower voltage limit (TC 8) resulted in more severe irreversible degradation associated with high delithiation of the SiO_x-containing graphite electrode. These conditions promoted mechanical degradation, SEI instability, lithium inventory loss, and increased impedance. In contrast, variations in charge C-rate resulted in comparatively small differences in degradation behaviour.

The electrochemical characterisation and post-mortem analyses showed strong agreement with the observed cycling behaviour. Cells exhibiting severe capacity fade also showed increased resistance, ICA peak shifts, peak broadening, and reduced peak intensity, indicating increased polarisation and interfacial degradation. Furthermore, the post-mortem analysis revealed highly heterogeneous ageing across the jellyroll. Different electrode regions within the same cell exhibited varying degrees of degradation, demonstrating that local mechanical stress, lithium distribution, and electrolyte accessibility strongly influenced the ageing behaviour. Visible Li-plating was not directly proportional to the observed capacity fade. Although Cell 15 exhibited more pronounced visible Li-plating than Cell 19, Cell 19 experienced substantially greater capacity loss, indicating that irreversible degradation processes contributed more significantly to the overall ageing behaviour than the visible amount of metallic lithium alone. The PAT-cell measurements further confirmed that local electrode regions aged differently within the same cell.

Finally, the in-house developed teardown tool substantially reduced the time required for cell disassembly and enabled a more efficient post-mortem analysis workflow. However, further refinement of the cutting depth control is required to prevent damage to the outer jellyroll layers during disassembly.

5.6 Future work

X-ray photoelectron spectroscopy (XPS) could be employed to further characterise the SEI composition and distinguish between different electrolyte decomposition products. In addition, cross-sectional SEM or focused ion beam (FIB) SEM analysis could provide more detailed information regarding electrode cracking, coating delamination, and the thicknesses of the electrode coatings and current collectors. X-ray diffraction (XRD) could also be utilised to investigate the structural properties and phase composition of the electrode materials. Furthermore, an additional test condition employing a 60% SOC window with a lower voltage limit close to 2.5 V could be investigated and compared with TC 8, which employed an 80% SOC window with a similar lower voltage limit. Such a comparison would help distinguish the influence of voltage window width from that of voltage window placement and could provide further insight into whether the SOC window size influences the electrode potentials and ageing behaviour. Further electrochemical testing should include a larger number of replicate cells for each test condition in order to improve the statistical reliability of the results. In addition, the teardown tool should be further refined to improve cutting depth control and minimise damage to the outer jellyroll layers.

References

[1] Bhat MY, Sofi AA, Ganie JA. Green wheels in motion: Electric vehicle sales in the path to decarbonization. Transportation Research Part D: Transport and Environment. 2025 5;142:104704. Available from: https://www.sciencedirect.com/science/article/pii/S1361920925001142.

[2] Pata SK, Erdogan S, Pata UK, Meo MS. Greening road transport: Comparison of technologies in conventional, hybrid, and electric vehicles. Journal of Environmental Management. 2025 4;380:124908. Available from: https://www.sciencedirect.com/science/article/pii/S0301479725008849.

[3] Qu B, Liang J, Huo D, Li H. Application of electrochemical methods in the recycling of spent lithium-ion batteries. Journal of Energy Storage. 2025 8;127:117180. Available from: https://www.sciencedirect.com/science/article/pii/S2352152X25018936.

[4] Berg H. Batteries for Electric Vehicles: Materials and Electrochemistry. Cambridge University Press; 2015.

[5] Group M. Micropower Group; 2026. Available from: https://micropower-group.com/about-us.

[6] Nölle R, Beltrop K, Holtstiege F, Kasnatscheew J, Placke T, Winter M. A reality check and tutorial on electrochemical characterization of battery cell materials: How to choose the appropriate cell setup. Materials Today. 2020 1;32:131-46. Available from: https://www.sciencedirect.com/science/article/pii/S1369702119307230.

[7] Qian C, Liu Y, Guo Z, Liu J, Chai F, Liu F. Research progress of SiOx anode materials modification strategy and its industrial application in lithium ion batteries. Materials Today Communications. 2025 1;42:111592. Available from: https://doi.org/10.1149/1945-7111/abe16b.

[8] Knorr J, Gomez-Martin A, Hsiao HC, Adam A, Rödl B, Danzer MA. Effect of different charge rates on the active material lithiation of Gr/SiOx blend anodes in lithium-ion cells. Journal of Energy Storage. 2024 5;86:111151. Available from: https://doi.org/10.3390/pr10112334.

[9] Yang X, Zhan C, Xu D, Nan D, Lv R, Shen W, et al. SiOx@Si-graphite microspheres for high-stable anode of lithium-ion batteries. Electrochimica Acta. 2022 9;426.

[10] Wang G, Cui N, Li C, Cui Z, Yuan H. A state-of-health estimation method based on incremental capacity analysis for Li-ion battery considering charging/discharging rate. Journal of Energy Storage. 2023 12;73:109010. Available from: https://www.sciencedirect.com/science/article/pii/S2352152X23024088.

[11] Inzelt G. Crossing the bridge between thermodynamics and electrochemistry. From the potential of the cell reaction to the electrode potential. ChemTexts. 2015 3;1.

[12] Birkl CR, McTurk E, Roberts MR, Bruce PG, Howey DA. A Parametric Open Circuit Voltage Model for Lithium Ion Batteries. Journal of The Electrochemical Society. 2015;162:A2271-80.

[13] Ovejas VJ, Cuadras A. Effects of cycling on lithium-ion battery hysteresis and overvoltage. Scientific Reports. 2019 12;9.

[14] Park S, Savvides A, Srivastava MB. Battery Capacity Measurement and Analysis using Lithium Coin Cell Battery; 2001.

[15] Altaf F. Thermal and State-of-Charge Balancing of Batteries using Multilevel Converters;.

[16] Killer M, Farrokhseresht M, Paterakis NG. Aging aware operation of lithium-ion battery energy storage systems: A review. Journal of Energy Storage. 2022 11;55:105634. Available from: https://doi.org/10.1016/j.apenergy.2019.114166.

[17] Soto A, Berrueta A, Mateos M, Sanchis P, Ursúa A. Impact of micro-cycles on the lifetime of lithium-ion batteries: An experimental study. Journal of Energy Storage. 2022 11;55:105343. Available from: https://doi.org/10.1109/tia.2021.3136808.

[18] Saxena S, Xing Y, Kwon D, Pecht M. Accelerated degradation model for C-rate loading of lithium-ion batteries. International Journal of Electrical Power & Energy Systems. 2019 5;107:438-45. Available from: https://www.sciencedirect.com/science/article/pii/S0142061518301212.

[19] Chang WY. The State of Charge Estimating Methods for Battery: A Review. ISRN Applied Mathematics. 2013 7;2013:1-7.

[20] Lai X, Ke Y, Tang X, Zheng Y. Balanced capacity-based quantitative method for detecting internal short circuits in Lithium-ion battery modules. Journal of Energy Storage. 2025 7;123:116622. Available from: https://www.sciencedirect.com/science/article/pii/S2352152X25013350.

[21] Gelam SD, Maddipatla S, Chicone C, Pecht M. Core collapse in cylindrical Li-ion batteries. Journal of Power Sources. 2024 12;623:235471. Available from: https://www.sciencedirect.com/science/article/pii/S037877532401423X.

[22] Yao XY, Pecht MG. Tab design and failures in cylindrical li-ion batteries. IEEE Access. 2019;7:24082-95.

[23] Han J, Li G, Zhu C, Wang Y, Fan G, Guo B, et al. Mechanism and analytical modeling of high-rate discharge aging in lithium-ion batteries: Emphasizing cathode current collector dissolution and particle fracture. Applied Energy. 2025 9;393:126048. Available from: https://www.sciencedirect.com/science/article/pii/S0306261925007780.

[24] Chen M, Zhang J, Ji X, Fu J, Feng G. Progress on predicting the electrochemical stability window of electrolytes. Current Opinion in Electrochemistry. 2022 8;34:101030. Available from: https://www.sciencedirect.com/science/article/pii/S2451910322000953.

[25] Takenaka N, Bouibes A, Yamada Y, Nagaoka M, Yamada A. Frontiers in Theoretical Analysis of Solid Electrolyte Interphase Formation Mechanism. John Wiley and Sons Inc; 2021.

[26] Hu D, Chen L, Tian J, Su Y, Li N, Chen G, et al. Research Progress of Lithium Plating on Graphite Anode in Lithium-Ion Batteries. Chinese Journal of Chemistry. 2021 1;39:165-73.

[27] Neubauer J, Pesaran A, Bae C, Elder R, Cunningham B. Fast charging of an electric vehicle lithium-ion battery at the limit of the lithium deposition process. Journal of Power Sources. 2019 7;427:260-70. Available from: https://doi.org/10.1016/j.jpowsour.2014.06.043.

[28] Scrosati B, Garche J. Modeling of lithium plating and lithium stripping in lithium-ion batteries. Journal of Power Sources. 2019 2;414:41-7. Available from: https://doi.org/10.1016/j.jpowsour.2009.11.048.

[29] Zhang Z, Pawar RD, Vidic RD. Study of thermodynamic models and crystallization kinetics for gypsum precipitation in hypersaline solutions with electrochemical impedance spectroscopy (EIS). Desalination. 2025 10;613:119025. Available from: https://www.sciencedirect.com/science/article/pii/S0011916425005016.

[30] Laschuk NO, Easton EB, Zenkina OV. Reducing the resistance for the use of electrochemical impedance spectroscopy analysis in materials chemistry. Royal Society of Chemistry; 2021.

[31] Yin L, Geng Z, Chien YC, Thiringer T, Lacey MJ, Andersson AM, et al. Implementing intermittent current interruption into Li-ion cell modelling for improved battery diagnostics. Electrochimica Acta. 2022 9;427:140888. Available from: https://www.sciencedirect.com/science/article/pii/S0013468622010477.

[32] Chien YC, Liu H, Menon AS, Brant WR, Brandell D, Lacey MJ. Rapid determination of solid-state diffusion coefficients in Li-based batteries via intermittent current interruption method. Nature Communications. 2023 12;14.

[33] Xu Z, Chen Z, Yang L, Zhang S. State of health estimation for lithium-ion batteries based on incremental capacity analysis and Transformer modeling. Applied Soft Computing. 2024 11;165:112072. Available from: https://www.sciencedirect.com/science/article/pii/S1568494624008469.

[34] Chowdhury NR, Smith AJ, Frenander K, Mikheenkova A, Lindström RW, Thiringer T. Influence of state of charge window on the degradation of Tesla lithium-ion battery cells. Journal of Energy Storage. 2024 1;76.

[35] Geng Z, Thiringer T, Lacey MJ. Intermittent Current Interruption Method for Commercial Lithium-Ion Batteries Aging Characterization. IEEE Transactions on Transportation Electrification. 2022 6;8:2985-95.

[36] Stroe DI, Swierczynski M, Stan AI, Teodorescu R, Andreasen SJ. Accelerated lifetime testing methodology for lifetime estimation of lithium-ion batteries used in augmented wind power plants. In: IEEE Transactions on Industry Applications. vol. 50. Institute of Electrical and Electronics Engineers Inc.; 2014. p. 4006-17.

[37] Weiss M, Mrzljak K, von Schmid M, Erbach G, Brierley N, Meisen T. Material-resolving computed tomography of lithium-ion batteries using deep learning.

NDT & E International. 2026 3;158:103565. Available from: https://doi.org/10.3390/ndt2030018.

[38] Houx JL, Kramer D. X-ray tomography for lithium ion battery electrode characterisation — A review. Energy Reports. 2021 5;7:9-14. Available from: https://doi.org/10.1146/annurev-matsci-070616-123957.

[39] Lumafield. Battery Quality Report;. Available from: https://www.lumafield.com/battery-report.

[40] Henini M. Scanning electron microscopy: an introduction. III-Vs Review. 2000 7;13:40-4. Available from: https://www.sciencedirect.com/science/article/pii/S096112900080006X.

[41] EPFL. EDX; 2025. Available from: https://www.epfl.ch/research/facilities/cmi/equipment/metrology/oxford-instruments-edx/.

[42] Saleh TA. 3D printing in analytical sample Preparation: A critical review of emerging tools, advantages, and challenges. Talanta. 2026 7;304:129546. Available from: https://doi.org/10.1016/j.teac.2020.e00101.

[43] Prusa. Types of printers and their differences; 2025. Available from: https://help.prusa3d.com/article/types-of-printers-and-their-differences_112464.

[44] Prusa. Polypropylene (PP); 2025. Available from: https://help.prusa3d.com/article/polypropylene-pp_167126.

[45] The PAT-Core concept | EL-CELL;. Available from: https://www.el-cell.com/pat-series/the-pat-core-concept/.

[46] Frenander K. Dynamic Battery Usage and its Effect on Degradation; 2025.

[47] Zhou G, Sun X, Li QH, Wang X, Zhang JN, Yang W, et al. Mn Ion Dissolution Mechanism for Lithium-Ion Battery with LiMn2O4 Cathode: In Situ Ultraviolet-Visible Spectroscopy and Ab Initio Molecular Dynamics Simulations. Journal of Physical Chemistry Letters. 2020 4;11:3051-7.

A
Appendix 1

Appendix A.1 Computed tomography scan

CT scan of Cell 11, including the top and bottom tab welds.

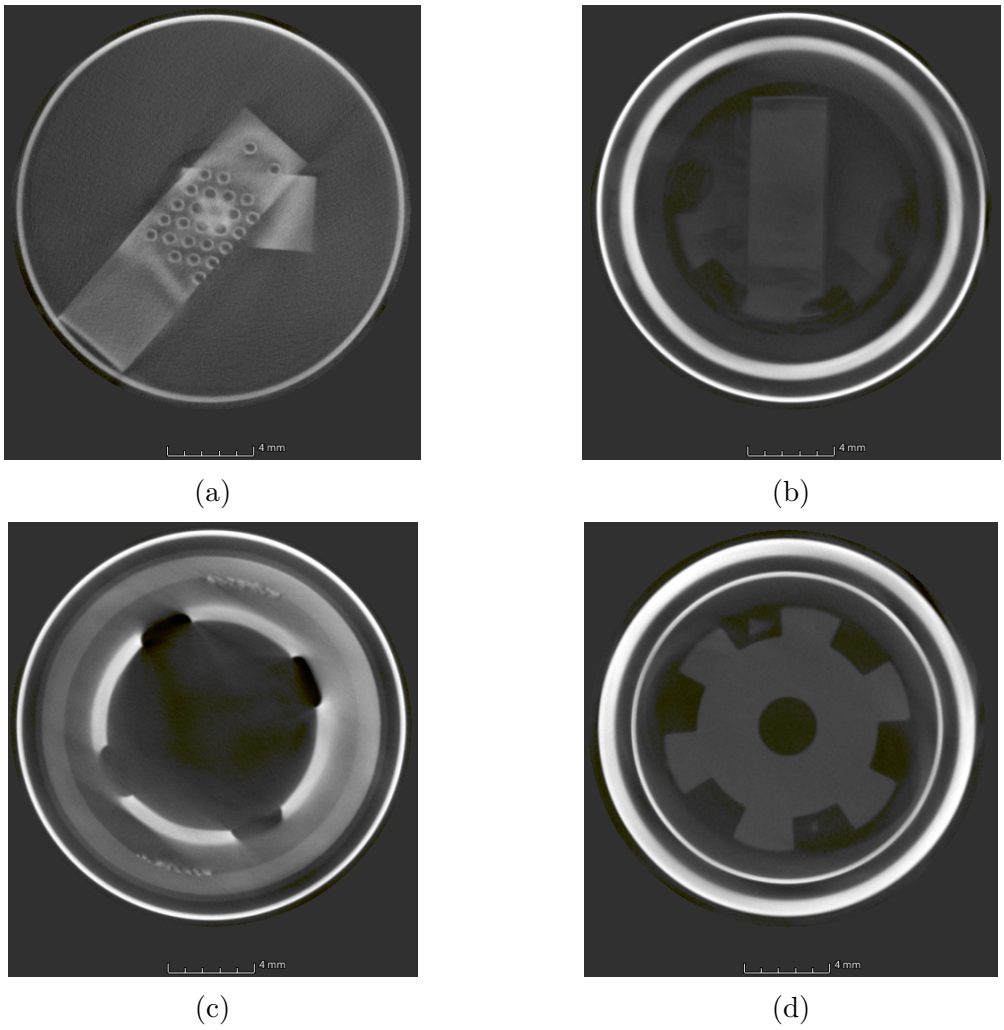

(a) (b)

(c) (d)

Figure A.1: (a) Bottom tab weld; (b) top tab; (c) top tab weld; (d) cap insulation structure (gear-shaped) of Cell 11.

B

Appendix 2

Appendix B.1 Post-mortem analysis

Appendix B.1.1 Scanning electron microscopy

SEM micrographs of the aged cells (Cells 11, 15, and 19) compared with the fresh reference cell (Cell 03) for the outer region of the negative electrode and the inner region of the positive electrode.

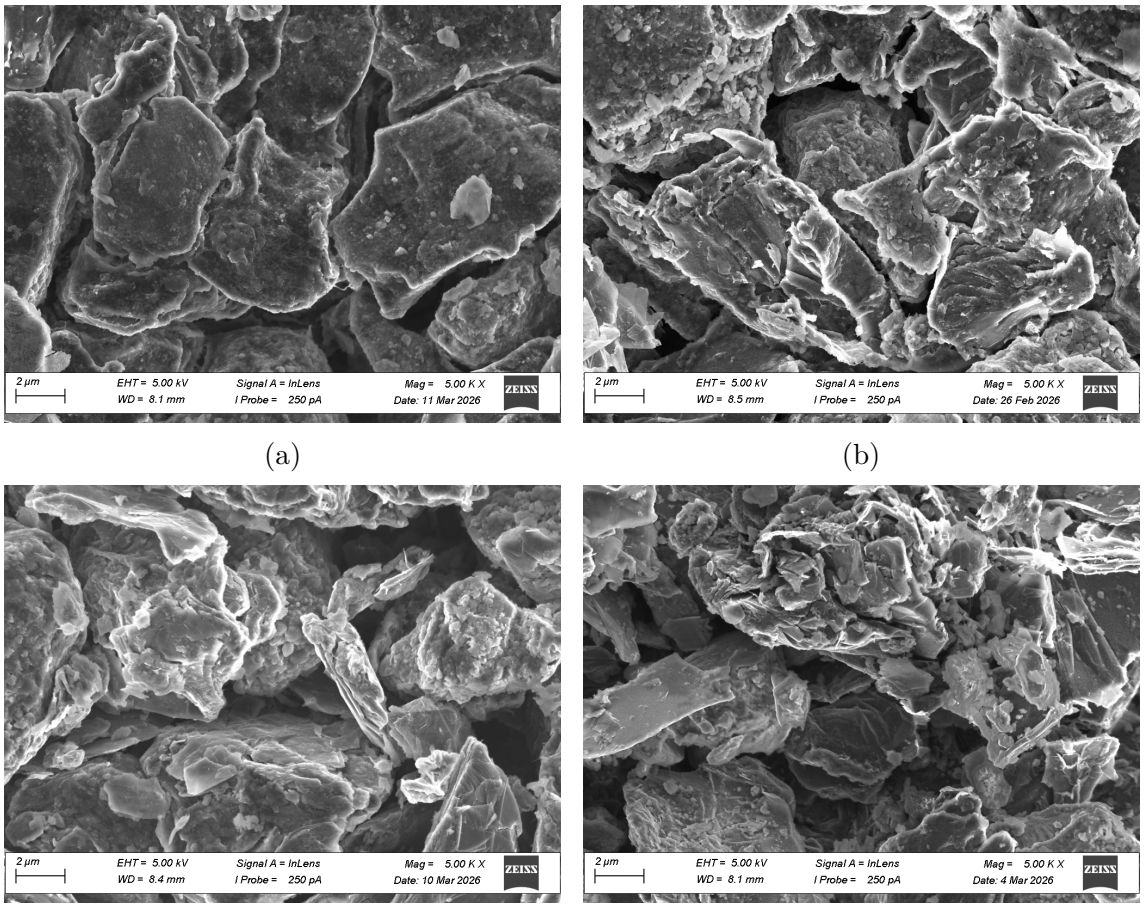

Figure B.1: SEM micrographs of the outer region of the negative electrode (graphite) for (a) Cell 03, (b) Cell 11, (c) Cell 15, and (d) Cell 19.

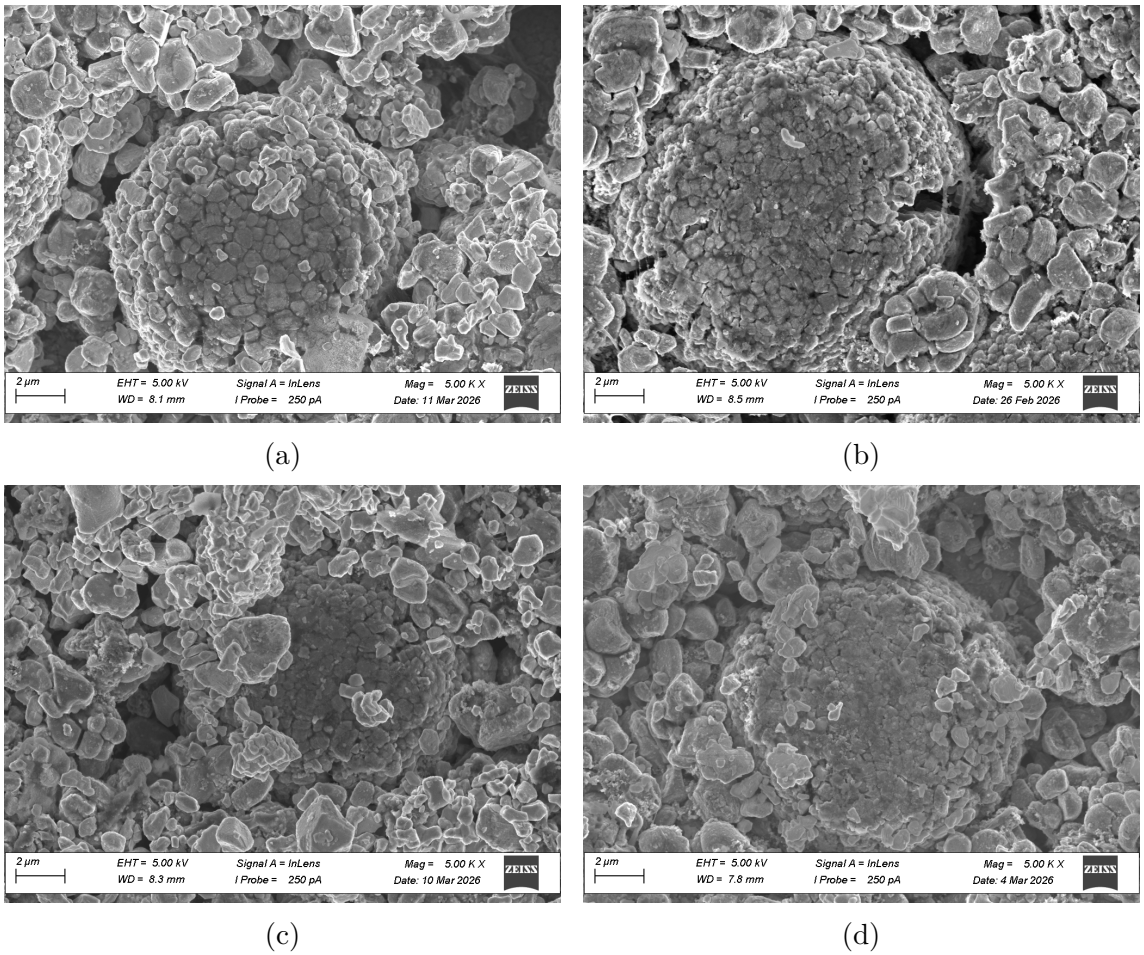

Figure B.2: SEM micrographs of the inner region of the positive electrode (NMC) for (a) Cell 03, (b) Cell 11, (c) Cell 15, and (d) Cell 19.

Appendix B.1.2 Energy dispersive X-ray spectroscopy

EDX mapping of Cell 11 for both the inner region of the negative electrode and the outer region of the positive electrode, together with the outer positive electrode region of Cell 15 and the inner negative electrode region of Cell 19.

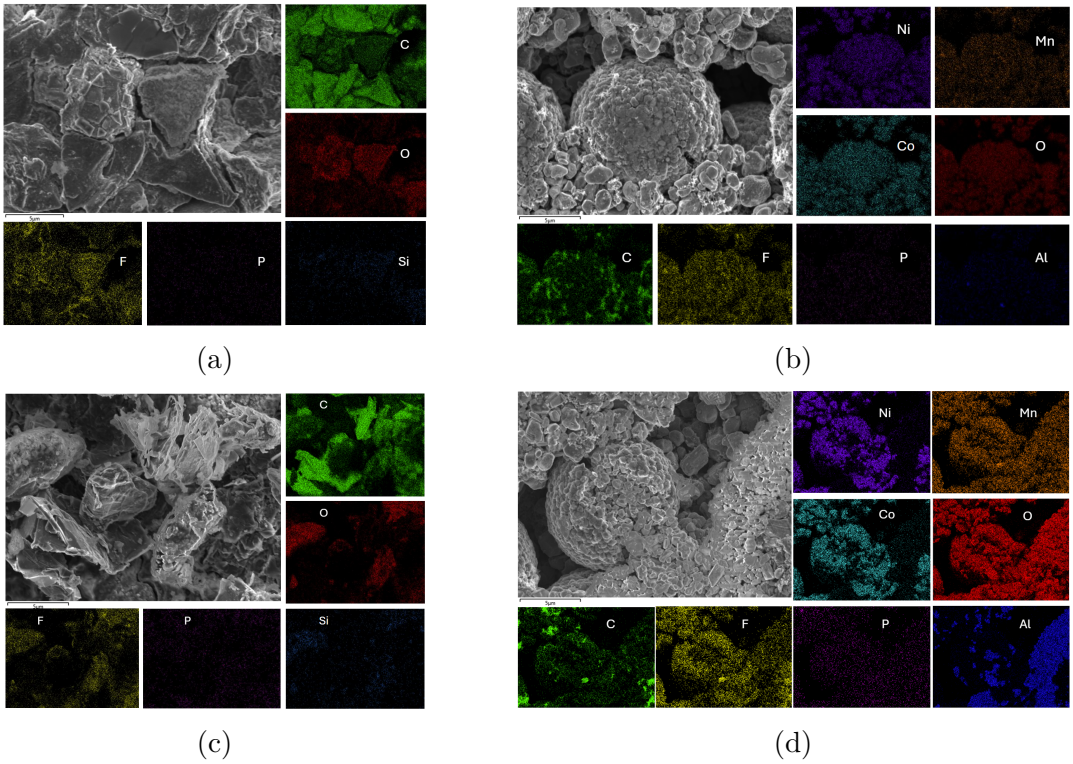

Figure B.3: EDX mapping of Cell 11 for (a) the negative electrode and (b) the positive electrode, together with (c) the negative electrode of Cell 19 and (d) the positive electrode of Cell 15.

Appendix B.1.3 Impedance analysis of PAT-cells

Nyquist plots at 50% SOC for the PAT-2 cells, including both the inner and outer regions of the negative and positive electrodes.

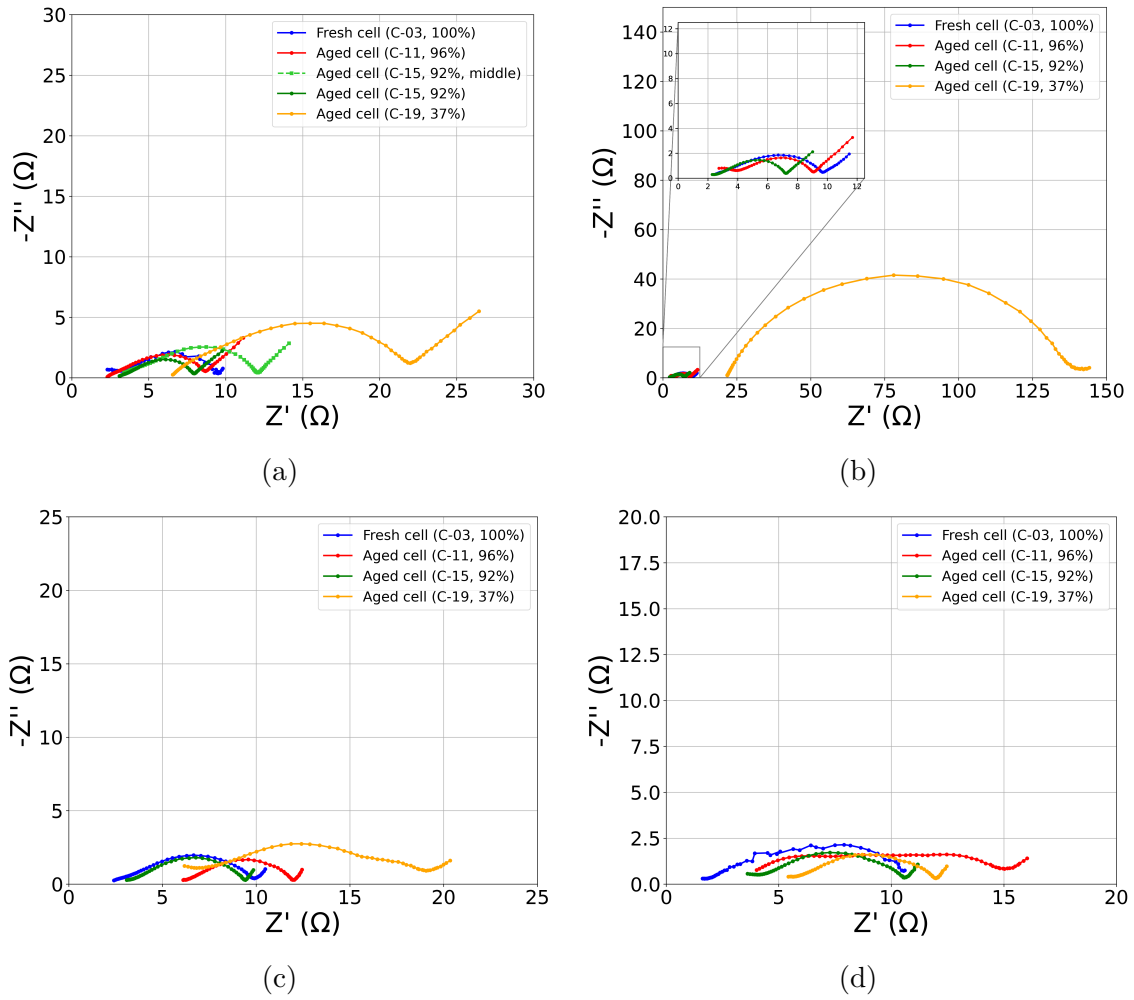

Figure B.4: EIS of Cell 03, 11, 15 and 19: (a) inner and (b) outer regions of the negative electrode for PAT-2; (c) inner and (d) outer regions of the positive electrode for PAT-2.

DEPARTMENT OF SOME SUBJECT OR TECHNOLOGY
CHALMERS UNIVERSITY OF TECHNOLOGY
Gothenburg, Sweden
www.chalmers.se

CHALMERS
UNIVERSITY OF TECHNOLOGY